SWELL3/SURGE: Computer Models for Hydrodynamic Response of MARK I Suppression Pools

EPRI

EPRI NP-835
Project 693-2
Final Report
June 1978

Keywords:
BWR
LOCA
Blowdown
Containment
Suppression Pool Hydrodynamics

Prepared by
JAYCOR
Del Mar, California

ELECTRIC POWER RESEARCH INSTITUTE

SWELL3/SURGE: Computer Models for Hydrodynamic Response of MARK I Suppression Pools

NP-835
Research Project 693-2

Final Report, June 1978

Prepared by

JAYCOR
1401 Camino Del Mar
P.O. Box 370
Del Mar, California 92014

Principal Investigators
Robert K.-C. Chan
Michael J. Vander Vorst

Prepared for

Electric Power Research Institute
3412 Hillview Avenue
Palo Alto, California 94304

EPRI Project Manager
Charles W. Sullivan
Nuclear Power Division

LEGAL NOTICE

FOREWORD

The initial goal of this project was to develop two-dimensional (2-D) computer programs to simulate, for a MARK I pressure suppression system, the pool swell surface shape and velocity prior to impact on structures. This effort has been coordinated with the MARK I Owner's Group to complement, in a timely manner, the efforts undertaken by that organization.

The generic research needs of the MARK I Group have evolved such that additional goals for the computer codes were established. The codes therefore evolved into more complex versions which will now predict: (1) vent clearing process; (2) three-dimensional (3-D) early bubble growth; (3) torus wall pressures; (4) net up and down loads on torus; (5) submerged velocity and acceleration fields; (6) pool surface shape and velocity prior to impact on structures; and (7) wet well pressurization. Predictions for a typical case are included at the end of this report with overall comparison with experimental data being good to excellent depending on the parameters chosen.

This EPRI project has been part of the MARK I Owner's Group program for addressing generic suppression system concerns and will complement additional generic EPRI experimental efforts underway to quantify pool swell effects in the MARK I pressure suppression system.

Future efforts will produce a user's manual to permit efficient use of these computer programs.

Charles W. Sullivan
Project Manager

ABSTRACT

This report describes in detail the analytical models, together with the computational techniques for their solution, that are used in a continuing effort to study the pool swell phenomenon in MARK I pressure suppression systems during a postulated LOCA. A calculation using 1/4-scale test conditions as input is given as an example.

CONTENTS

Section — Page

1. INTRODUCTION 1-1

2. SWELL3—MODEL FOR THREE-DIMENSIONAL BUBBLE FLOW 2-1
   2.1 Mathematical Model for the Flow 2-4
      Eulerian-Lagrangian Discretization 2-5
   2.2 Vent Clearing Model 2-6
   2.3 Bubble Formation Model 2-10
      Numerical Solution 2-11
      Velocity Calculation 2-24
      Pressure, Load, and Impulse on Torus 2-25
   2.4 SWELL3 MODEL SUMMARY 2-28

3. SURGE—MODEL FOR TWO-DIMENSIONAL POOL SWELL 3-1
   3.1 The GALE Method 3-1
   3.2 Mesh Generation, Rezoning, and Smoothing 3-10
   3.3 Transition from SWELL3 to SURGE 3-13
   3.4 Solution of the Pressure Field 3-17

4. MODEL FOR FLOW IN THE VENT SYSTEM AND BUBBLES 4-1
   4.1 Derivation of Governing Equations 4-1
   4.2 Numerical Solution Procedure 4-5

5. SAMPLE CALCULATION 5-1

6. REFERENCE 6-1

APPENDIX A-1. SUCCESSIVE OVER-RELAXATION A1-1

APPENDIX A-2, FORMATION OF IRREGULAR STARS A2-1

APPENDIX A-3. SOME GEOMETRIC IDENTITIES INVOLVING TRIANGLES A3-1

LIST OF FIGURES

Figure		Page
2.1	MARK I Containment Schematic	2-2
2.2	MARK I BWR Containment Pool Swell 1/4 Scale Test Facility—Perspective	2-3
2.3	Definition of Variables and Boundary Conditions for VENT3 and SWELL3 Formulation	2-8
2.4	Schematic of a Single-Cell Suppression Vessel Model	2-12
2.5	Mesh Configuration for SWELL3 Simulations	2-13
2.6	Pool Surface Perspective	2-14
2.7	Initial Bubble Surface at Exit of Downcomer	2-16
2.8	Bubble at Exit of Downcomer	2-17
2.9	Cross-Sections of Finite Difference Mesh Showing Bubble Surface	2-18
2.10	Irregular Star in a Two-Dimensional Space	2-20
2.11	Three-Dimensional Irregular Star	2-20
2.12	Velocity Extrapolation in a Two-Dimensional Space	2-26
2.13	Surface Points Used to Determine the Normal at p_s	2-26
3.1(a)	Schematic of the SURGE Mesh	3-2
3.1(b)	SURGE Mesh in the Lagrangian Space	3-2
3.2	Control Volume for an Interior Vertex (i,j)	3-3
3.3	Control Volume for a Boundary Vertex	3-5
3.4	Illustration of the Rezoning Procedure	3-5
3.5	Generation of Initial Conditions for a SURGE Run	3-15
4.1	Schematic of the Compressible Gas Flow Model	4-2
5.1	Bubble and Pool Surface Plots from SWELL3 for Case GE 1-21 . . .	5-2
5.2	Bubble and Pool Surface Plots from SURGE for Case GE 1-21 . . .	5-3
5.3	Pressures, Load, and Impulse for Case GE 1-21	5-4
5.4	Pool Surface Displacements, Bubble Surface Profiles, and Pool Surface Velocities from SURGE for Case GE 1-21	5-5

EXECUTIVE SUMMARY

This report is a detailed documentation of the analytical models, and the corresponding solution procedures, that are employed in a continuing investigation of the pool swell in MARK I pressure suppression systems during a postulated LOCA. The present study is concerned with the vent clearing and the subsequent pool swell resulting from the pressurization of the drywell with air. Steam condensation is outside the scope of this work.

The computer codes SWELL3 and SURGE, which are based on the formulations described in this report, have been used in validations against 1/4-scale and 1/12-scale laboratory experiments. Since the validations are still being evaluated, they will not be included here. Nevertheless, a typical simulation run, using 1/4-scale test configuration as input, is given as an example.

Section 1

INTRODUCTION

This report documents in detail the analytical models, together with the computational techniques for their solution, that are employed in a continuing effort to study the pool swell phenomenon in MARK I pressure suppression systems during a postulated loss-of-coolant accident (LOCA).

The events following a postulated LOCA are numerous: the discharging of high-pressure steam into the drywell which in turn forces a mixture of air and steam into the vent system; the pool swell in response to the flow of air into the bubbles; and condensation of steam in the suppression pool. The present study is concerned with the development of computational tools for simulating the vent clearing process and the subsequent phenomenon of pool swell that result from the pressurization of the drywell with air. Steam condensation is outside the scope of this investigation.

As discussed in an earlier report [1], our approach has been to distinguish two-dimensional flow regime from the three-dimensional one, and to use computational techniques appropriate for each regime. The two regimes are: the essentially three-dimensional flow field during and shortly after the vent-clearing process, and the approximately two-dimensional flow in the later stages of bubble growth. In an earlier study [1], the VENT3 code was used to cover the period from the onset of drywell pressurization to the instant when water in the downcomer is completely expelled. After vent clearing, the simulation of pool response was performed using the two-dimensional SURGE code. By comparing with Stanford Research Institute's 1/10-scale test measurement, the predictions on pool surface displacement and velocity by VENT3 and SURGE were quite good. It was found later, however, that the VENT3/SURGE model is not adequate for predicting the peak download on the torus, which occurs shortly after vent clearing. The reason is that the two-dimensional SURGE code cannot properly describe the flow field about a highly three-dimensional bubble which is just being formed. In order to treat this flow regime adequately, a time-dependent, three-dimensional code (SWELL3) has been developed; SWELL3 includes VENT3 as a submodel for the vent clearing process as before.

In what follows, detailed descriptions of the mathematical formulations and solution procedures for SWELL3 (Section 2) and SURGE (Section 3) are given. Section 4 describes the equations for modeling the pressure drop in the vent system; and an example using General Electric Company's 1/4-scale test conditions as input is given in Section 5.

Section 2

SWELL3—MODEL FOR THREE-DIMENSIONAL BUBBLE FLOW

The SWELL3 computer code calculates the fully three-dimensional fluid flow during vent clearing and the flow associated with the formation and growth, at early times, of the underwater bubble. This section presents the numerical method contained in the SWELL3 code to simulate three-dimensional flows bounded by rigid walls and multiple free surfaces which are not restricted in their orientation.

Boiling water reactors incorporate in their design a pressure suppression system. The MARK I containment design shown in Figure 2.1 is essentially a large pool of water contained by a toroidal vessel. During a postulated loss-of-coolant accident, steam from the depressurizing reactor mixes with air and is vented through "vent pipes" from the reactor drywell into the wetwell. These vent pipes lead to a toroidal ring header which is contained within the main torus and is located above the pool surface. Pairs of pipes called downcomers lead from the ring header and extend vertically downward into the pool with their exit openings below the pool surface. Figure 2.2 shows a schematic of the quarter-scale test facility for modeling a cross section of the pressure suppression system during a postulated LOCA. It contains one pair of downcomers in a cylindrical vessel. The SWELL3 computer code simulates the incompressible fluid flow in a wetwell configuration similar to this experimental model.

Before the sub-scale experiment begins, the large air reservoir is pressurized and pressures in the wetwell airspace and drywell are reduced to about 1/4 of the atmospheric pressure. The wetwell and drywell are either at the same pressure (the so-called zero Δp condition), in which case the water in the downcomer pipe is at the same level as the water in the pool, or the drywell pressure is slightly larger (the full Δp condition) so that the water level in the downcomer is initially at the exit of the pipe. The initiation of the event begins when a diaphragm between the reservoir and the drywell is broken, allowing air to flow into the drywell and then through the vent pipes and the ring header into the downcomers. The water in the downcomers is forced down, and eventually the air

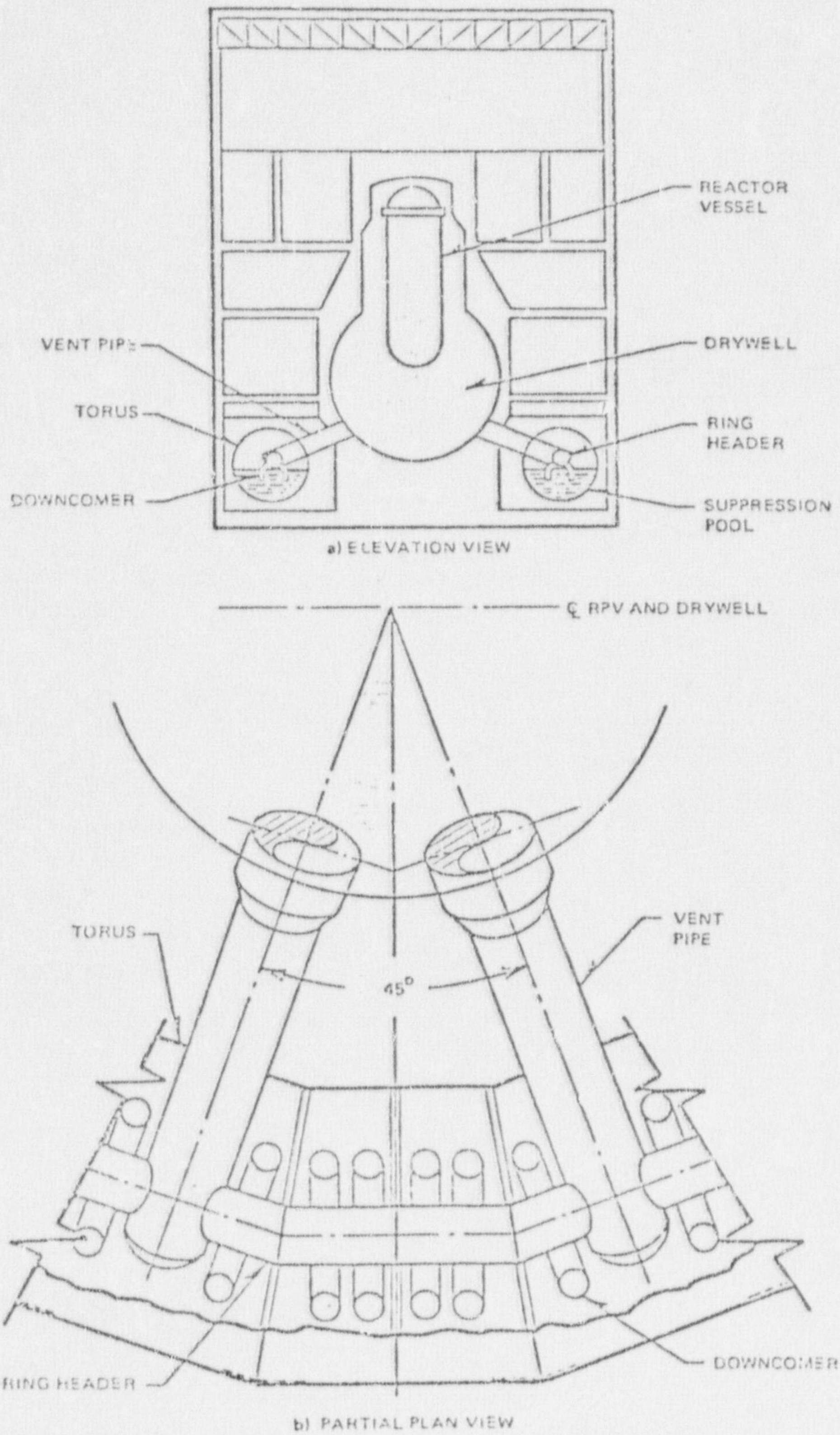

Figure 2.1. MARK I Containment Schematic

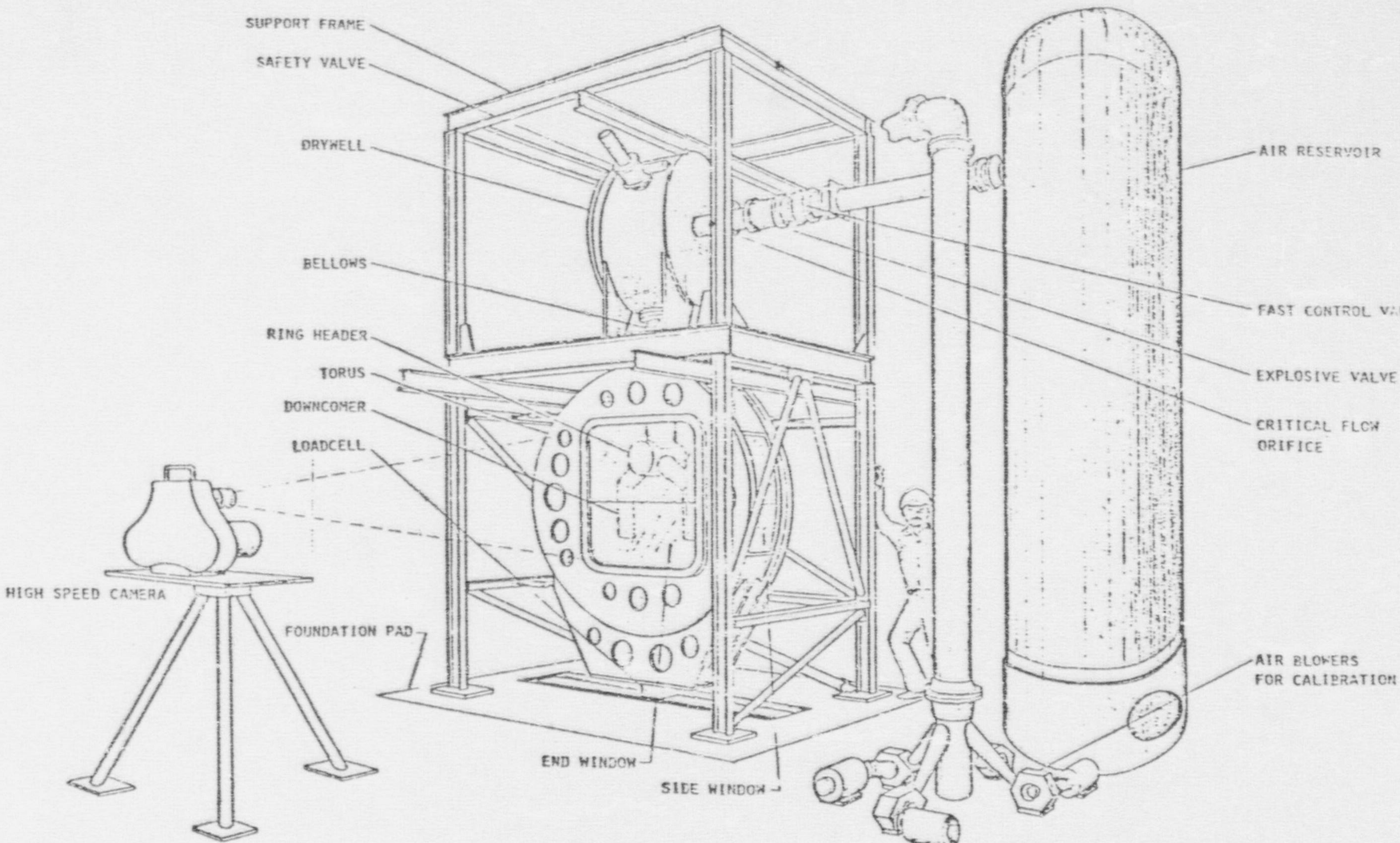

Figure 2.2 MARK I BWR Containment Pool Swell 1/4 Scale Test Facility—Perspective

is vented into the pool where an underwater bubble is formed at the exit of each downcomer. The torus wall experiences a certain amount of downward dynamic load (the "down-load") during vent clearing and the early stages of the bubble growth, the maximum magnitude occuring just after vent clearing. During this time the pool surface displacement is so small that the pressure in the wetwell airspace, which is sealed in, changes little. After vent clearing, the pressure loss in the vent system, consisting of the vent pipe, ring header, and downcomers, is such that the bubble pressure and the corresponding torus load begin to decrease although the drywell pressure is still increasing. At later times the rising pool surface causes the wetwell airspace volume to decrease, therefore, increasing the airspace pressure. The net dynamic load on the torus may become upward after the water in the pool has gained a certain amount of upward momentum, which in turn exerts on the upper half of the torus wall through the rising pressure in the airspace.

In an earlier study [1], the VENT3 code was used to calculate the flow during the vent clearing process. After vent clearing, the purely two-dimensional SURGE code was used for the bubble growth and the associated pool swell. As demonstrated in Reference 1, the predictions on pool surface velocity and displacement were in good agreement with Stanford Research Institute's 1/10 scale experiments. It was found later, however, that the peak download, occuring just after vent clearing, can not be correctly calculated by using a purely two-dimensional model such as SURGE for the early growth of the bubble, which is characterized by highly three-dimensional effects. To treat this flow regime properly, the SWELL3 code was developed; it contains VENT3 as a module for the vent clearing process. The bulk of SWELL3, however, deals with the fully three-dimensional, time-dependent problem of tracing the evolution of the bubble and the corresponding flow field.

In the following subsections, descriptions will be given of the underlying assumptions regarding the flow and the geometry, followed by separate descriptions of the vent clearing model and the bubble formation model. The vent clearing model is essentially the same as VENT3 in Reference 1, but a different approach is taken as far as the derivation is concerned.

2.1 MATHEMATICAL MODEL FOR THE FLOW

Potential flow has been assumed for the basic mathematical model of the fluid flow. With the possible exception of the flow at the exit of the downcomer, the assumptions of irrotational, inviscid flow are adequate for the solution of this geometrically complex problem throughout the flow regime. During the process of vent clearing, the flow around the edges of the downcomer is turbulent. The resulting turbulent "turning" losses are approximated within the potential flow model by assuming that there is a pressure drop across the end of the downcomer which is proportional to the square of the exit velocity.

The assumption of potential flow avoids several difficulties which would occur if we were to solve the system of equations arising from the Navier-Stokes equations using the primitive variables of pressure and velocity. From the numerical point of view, we need computer storage for only one primary variable, the potential ϕ. Even with the power of today's computers, the resolution of a three-dimensional, finite difference mesh in the primitive variables is severely limited. Second, the primitive equations are difficult to integrate in time on an Eulerian finite difference mesh with irregular boundaries. The usual simple schemes require the addition of a numerical diffusion, either explicit of implicit, whereas neutrally stable schemes are difficult to implement for free surface flows with irregular geometries. Third, using potential flow, only $\nabla\phi$ needs to be accurately approximated on free surfaces. With the primitive equations, however, many more combinations of velocity derivatives are needed to evaluate the convective terms in the momentum equations and the source term in the Poisson equation for the pressure. All of these derivatives are difficult to calculate near free surfaces.

The major disadvantage of solving for the potential in a finite difference formulation instead of directly solving for the velocity and pressure is that it is necessary to take derivatives of the resulting discrete potential solution to obtain the variables of interest. To calculate the velocity, we need to compute the spatial first derivatives $\vec{\nabla}\phi$; to compute the pressure we need the first time derivative $\frac{\partial\phi}{\partial t}$, in addition to the velocity; and to compute the acceleration we need the second derivatives $\frac{\partial}{\partial t}\vec{\nabla}\phi$. Direct numerical differentiation of the potential obtained by the procedure developed in the succeeding sections yields sufficiently accurate velocities and pressures. However, the acceleration obtained by direct numerical differentiation of the discrete potential solution is quite noisy. For a fixed point in space, a smooth acceleration-versus-time profile can be obtained by approximating the time history of velocity potential at that point by cubic spline. The accuracy of the resulting acceleration, however, has not been fully established.

Eulerian-Lagrangian Discretization

The flow equations are written in a mixed Eulerian-Lagrangian system. The free surfaces are moving through a fixed three-dimensional rectangular finite difference mesh. In the fluid interior, the equations are written with respect to a fixed (Eulerian) computational mesh. However, on the free surface, they are written with respect to the moving (Lagrangian) surface. Moreover, at interior points which are close to a free surface, the flow equations are discretized by an "irregular star" technique using the values of the potential at both interior and surface points, but involving no points which lie outside of the flow regime. Similarly, when a spatial derivative at a free surface point is needed, it is evaluated by one-sided differencing so that no points outside of the fluid region need to be used.

Considerations of the compromise between computer storage and accuracy requirements were primary in the choice of the mixed Eulerian-Lagrangian formulation as opposed to a strictly Eulerian or strictly Lagrangian approach. In terms of accuracy, a totally Lagrangian treatment of the entire three-dimensional flow region might be preferable. However, the computer storage required to obtain the necessary cell resolution for such a scheme would be exorbitant. On the other hand, a strictly Eulerian method similar to a primitive Marker-And-Cell method, in which the free surfaces are approximated by rectangular steps, was initially attempted and found to be too inaccurate in its prediction of torus wall pressures. The storage requirements of the mixed Eulerian-Lagrangian formulation are not much larger than the purely Eulerian approach. However, since it uses the exact position of the free surface within the underlying rectangular mesh, higher accuracy can be achieved.

2.2 VENT CLEARING MODEL

In the interval from the time of initial drywell pressurization to the time when the downcomer vent clears, it is shown in Reference 1 that a simple model can yield good results. For completeness this vent clearing model (VENT3) is also described here.

The following assumptions are made:

(1) The water exits the downcomer with uniform velocity $w(t)$ across its cross section.

(2) The potential vanishes on the pool surface.

(3) There is an average pressure drop proportional to $\frac{1}{2}\rho w^2$ across the exit of the downcomer, where the loss coefficient f is obtained empirically.

Justification of these assumptions was given in Reference 1.

A summary of the equations to be solved during vent clearing is the following:

$$\nabla^2\phi = 0 \text{ (interior of the pool)} \tag{2-1}$$

$$\frac{\partial\phi}{\partial n} = 0 \text{ (rigid boundaries)} \tag{2-2}$$

$$\phi = 0 \text{ (pool surface)} \tag{2-3}$$

$$\frac{\partial\phi}{\partial z} = w(t) \text{ (downcomer exit)} \tag{2-4}$$

where an expression for w is yet to be determined. Now if we let $\phi^*(x,y,z)$ be the solution of the strictly spatial boundary-value problem

$$\nabla^2\phi^* = 0 \text{ (interior)} \tag{2-5}$$

$$\frac{\partial\phi^*}{\partial n} = 0 \text{ (rigid boundaries)} \tag{2-6}$$

$$\phi^* = 0 \text{ (pool surface)} \tag{2-7}$$

$$\frac{\partial\phi^*}{\partial z} = -1 \text{ (downcomer exit)} \tag{2-8}$$

then

$$\phi(x,y,z,t) = -w(t)\phi^*(x,y,z) \tag{2-9}$$

satisfies Equations (2-1) through (2-4).

Next consider the problem of matching the three dimensional flow in the pool with the one dimensional flow in the downcomer, that is, finding the function $w(t)$. Referring to Figure 2.3 for nomenclature, let $p_1(t)$ be the pressure applied to the water surface in the downcomer, $p_2(t)$ the fluid pressure just above the downcomer exit, $p_3(t)$ the average fluid pressure in the pool just below the exit of the downcomer. Furthermore, let $h(t)$ be the length of the water column in the downcomer, and A the constant cross-sectional area of the downcomer. Now consider the conservation of vertical momentum in the control volume formed by the water in the downcomer. In this control volume the time rate of change of momentum is

$$\frac{d}{dt}\left[\rho A h\, w\right] - (\rho A w)w$$

where ρ is the density of water and the second term is the flux of momentum through the downcomer exit. This rate of change of momentum is balanced by the sum of the surface forces due to the pressure $(p_2 - p_1)A$, and the body force $-\rho hAg$ due to gravity. Summing these contributions, and differentiating, we have

$$\frac{dw}{dt} = \frac{1}{h}\left[\frac{p_2 - p_1}{\rho}\right] - g \quad . \tag{2-10}$$

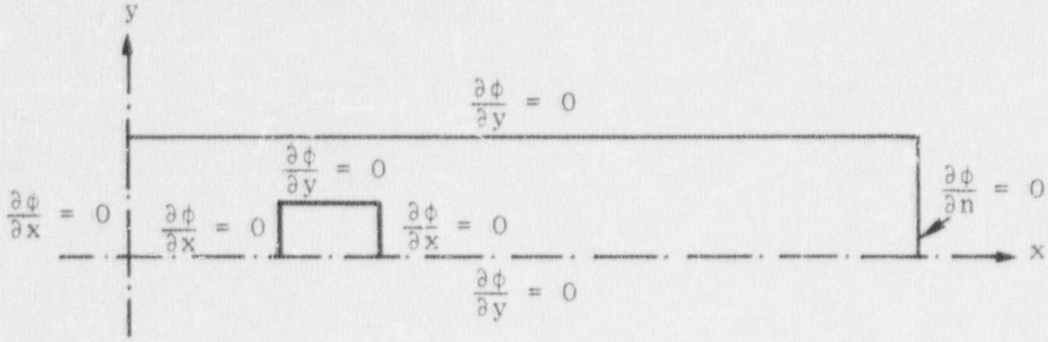

(a) Top View

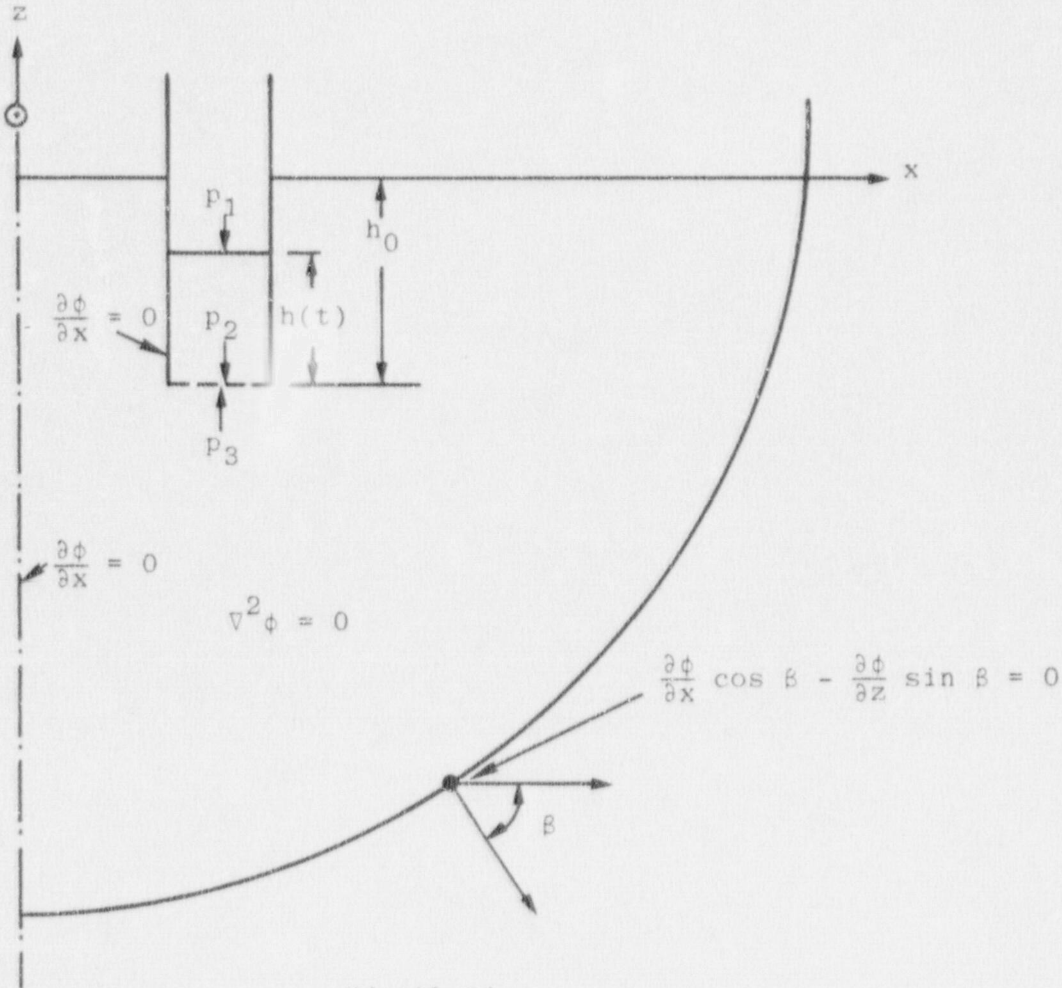

(b) Side View

Figure 2.3. Definition of Variables and Boundary Conditions for VENT3 and SWELL3 Formulation

From assumption (3), p_2 is related to p_3, the average pressure in the pool just below the exit of the downcomer, by

$$p_2 = p_3 + \frac{1}{2}f\rho w^2$$
$$= \frac{1}{A}\int p dA + \frac{1}{2}f\rho w^2 \qquad (2\text{-}11)$$

where the integration is taken just below the downcomer exit.

The Bernoulli equation can be written

$$\frac{\partial\phi}{\partial t} + \frac{1}{2}(u^2 + v^2 + w^2) + \frac{p - p_{air}}{\rho} + g(z - z_0) = 0 \qquad (2\text{-}12)$$

where p_{air} is the wetwell airspace pressure, (u,v,w) the components of the velocity vector, g the gravitational acceleration, and z_0 the elevation of the undisturbed free surface.

Applying Equations (2-9), (2-11), and (2-12) at point 3 (Figure 2.3), neglecting $(u^2 + v^2)$ which is much smaller than w^2 throughout most of the downcomer exit, we obtain

$$p_2 = p_{air} + \rho\left[\frac{1}{\alpha}\frac{dw}{dt} - \frac{1-f}{2}w^2 + gh_0\right] \qquad (2\text{-}13)$$

where h_0 is the submerged length of the downcomer; the constant α is determined from the solution of the ϕ^* field, formulated in Equations (2-5) to (2-8), by

$$\frac{1}{\alpha} = \frac{1}{A}\int_{\text{downcomer exit}} \phi^* dA \qquad (2\text{-}14)$$

Eliminating p_2 between Equations (2-10) and (2-13) we obtain the desired expressions

$$\frac{dw}{dt} = \frac{\alpha}{1-\alpha h(t)}\left[\frac{p_1(t) - p_{air}}{\rho} + \frac{1-f}{2}w(t)^2 + g(h(t) - h_0)\right] \qquad (2\text{-}15)$$

where

$$\frac{dh}{dt} = w(t) \quad . \qquad (2\text{-}16)$$

In summary, to solve for the potential ϕ during vent clearing, first solve the system represented by Equations (2-5) to (2-8) for ϕ^*; use Equation (2-14) to find α; use the applied drywell pressure with adjustment for vent system losses (see Section 4) to find p_1 and solve the system of first order ordinary differential equations (2-15) and (2-16) for w(t). Equation (2-9) then gives the velocity potential in terms of ϕ^* and [illegible]. The numerical procedures for solving for ϕ^* and $w(t)$ were presented in considerable detail in our previous work [1]; they will not be repeated here.

2.3 BUBBLE FORMATION MODEL

The assumptions of frictionless, irrotational, incompressible flow imply that the velocity, $\vec{U} = (u,v,w)$, can be derived from a scalar potential function $\phi(x,y,z,t)$ by

$$\vec{U} = \nabla\phi \tag{2-17}$$

where ϕ satisfies

$$\nabla^2\phi = 0 \quad . \tag{2-18}$$

On free surfaces the potential must satisfy the Bernoulli equation, and on fixed, solid boundaries the normal component of velocity vanishes, i.e.,

$$\frac{\partial\phi}{\partial n} = 0 \quad . \tag{2-19}$$

At vent clearing the surface of the bubble is assumed to be a flat sheet at the exit of downcomer. On the bubble surface the Lagrangian form of the Bernoulli equation applies:

$$\frac{d\phi}{dt} = \frac{1}{2}(u^2 + v^2 + w^2) - \frac{p_{bub} - p_{air}}{\rho} - g(z - z_0) \tag{2-20}$$

where p_{bub} is the uniform pressure on the bubble. The left-hand side of Equation (2-20) denotes the time rate of change of ϕ following a water particle on the bubble surface. On the pool surface in contact with the airspace of the wetwell, the motion of free surface is represented by mesh points that are allowed to move only in the vertical direction. At these points the applicable form of [illegible]rnoulli equation is

$$\frac{d\phi}{dt} = \frac{1}{2}(w^2 - u^2 - v^2) - g(z - z_0) \tag{2-21}$$

where $\frac{d\phi}{dt}$ is the rate of change of ϕ following these special points.

At a fixed interior point the applicable Bernoulli equation is of the familiar form

$$\frac{\partial\phi}{\partial t} + \frac{1}{2}(u^2 + v^2 + w^2) + \frac{p - p_{air}}{\rho} + g(z - z_0) = 0 \tag{2-22}$$

In addition we assume that the pressures are equal in the two downcomers throughout the event. Then since the geometry (Figure 2.4) is symmetrical with respect to the two vertical planes which bisect the cylinder, the calculation need only be done in one quadrant as shown in Figure 2.3. The boundary conditions on planes of symmetry are the same as if they were rigid walls; that is, the normal component of velocity, $\frac{\partial\phi}{\partial n}$, vanishes.

Numerical Solution

The primary components of the numerical procedure employed in this work are the use of three-dimensional irregular stars to represent the Laplacian operator in Equation (2-18) and the evaluation of the instantaneous velocities on the bubble surface by a linear extrapolation from two interior points along a direction normal to the surface. The technique of irregular stars was used by Chan and Street [2] in their numerical study of two-dimensional, large-amplitude water waves. Subsequently, the same technique or variants of it have been successfully used by other investigators. Vander Vorst and Van Tuyl [3] used the irregular star technique for the solution of the motion of a two-dimensional underwater bubble. They also demonstrated the usefulness of determining free surface velocity by extrapolation along lines normal to the surface. Due to the complexity of the computations, neither of these concepts have been previously extended to three-dimensional flows with free surfaces of arbitrary orientation.

The computational fluid region is that bounded by the pool surface, $\xi(x,y)$, and the bubble surface as shown in Figure 2.5. The circular cylindrical downcomers are replaced by rectangular ones with the same cross-sectional area. In addition, the circular arc defining the torus wall is approximated by the step-like profile which follows the boundaries of computational cells.

Values of the potential $\phi_{i,j,k} = \phi(x_i, y_j, z_k)$ are defined at the intersections of the mesh lines, i.e., at cell corners. There are two different free surface representations, one for the pool surface and one for the bubble. We assume that the pool surface can be represented by a single-valued displacement function $\xi = \xi(x,y)$ or in terms of the finite difference mesh, $\xi_{i,j} = \xi(x_i, y_j)$, and we also define $\phi_{\xi,i,j} = \phi(x_i, y_j, \xi_{i,j} + z_0)$ as shown in Figure 2.6. Since the bubble undergoes large deformations, it cannot be characterized by such a simple relationship. Instead we use a parametric representation for the coordinates $R = (x,y,z)$ of the bubble where

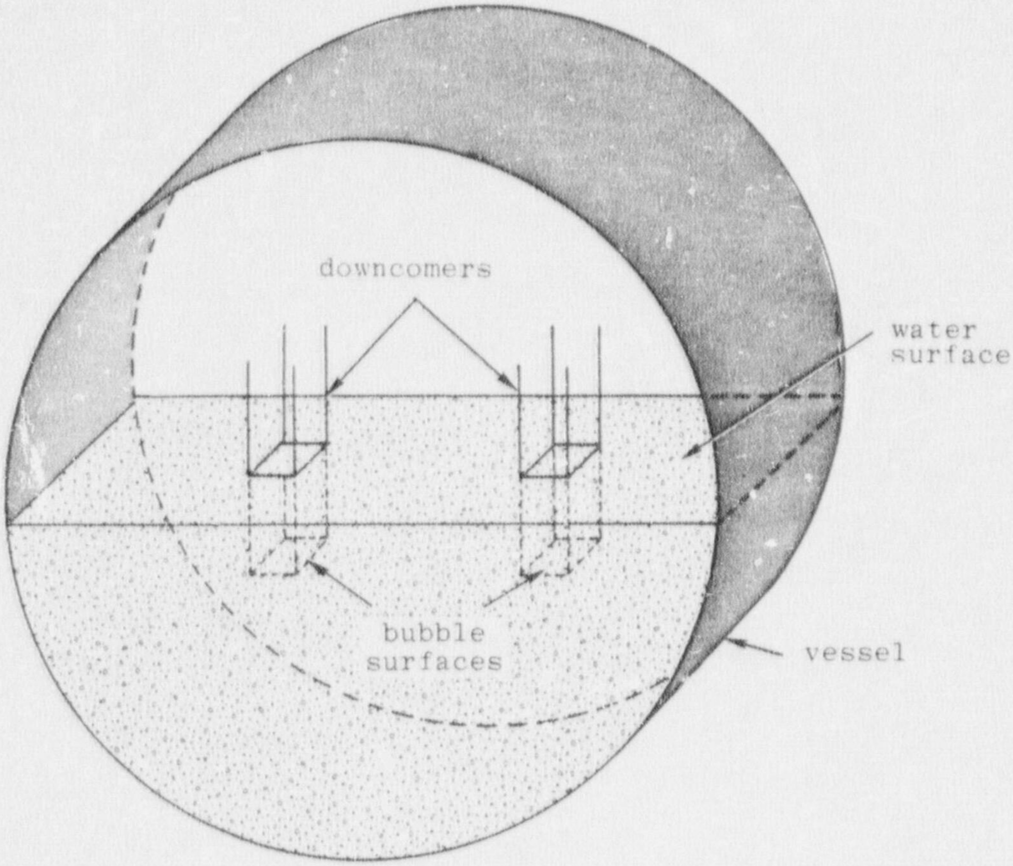

Figure 2.4. Schematic of a Single-Cell Suppression Vessel Model (Circular Cylindrical Downcomers are Replaced by Rectangular Ones)

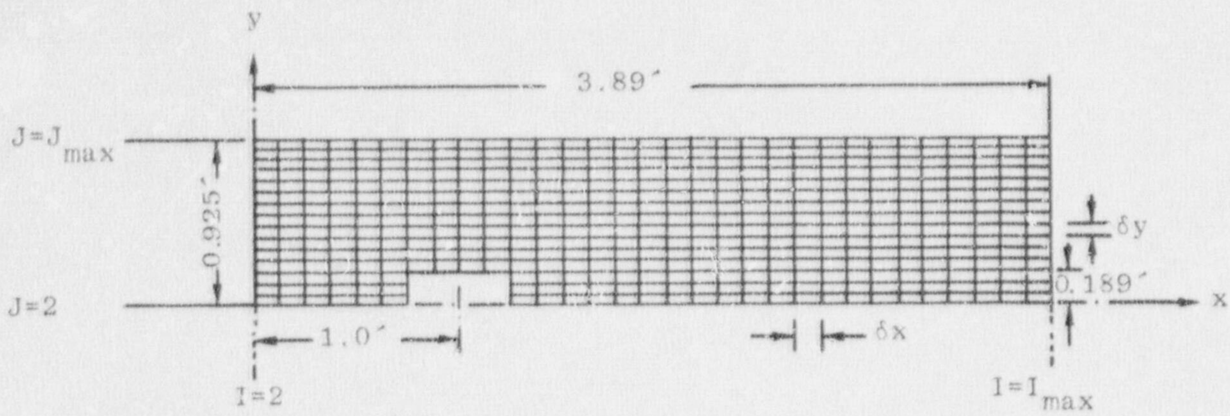

(a) Top View

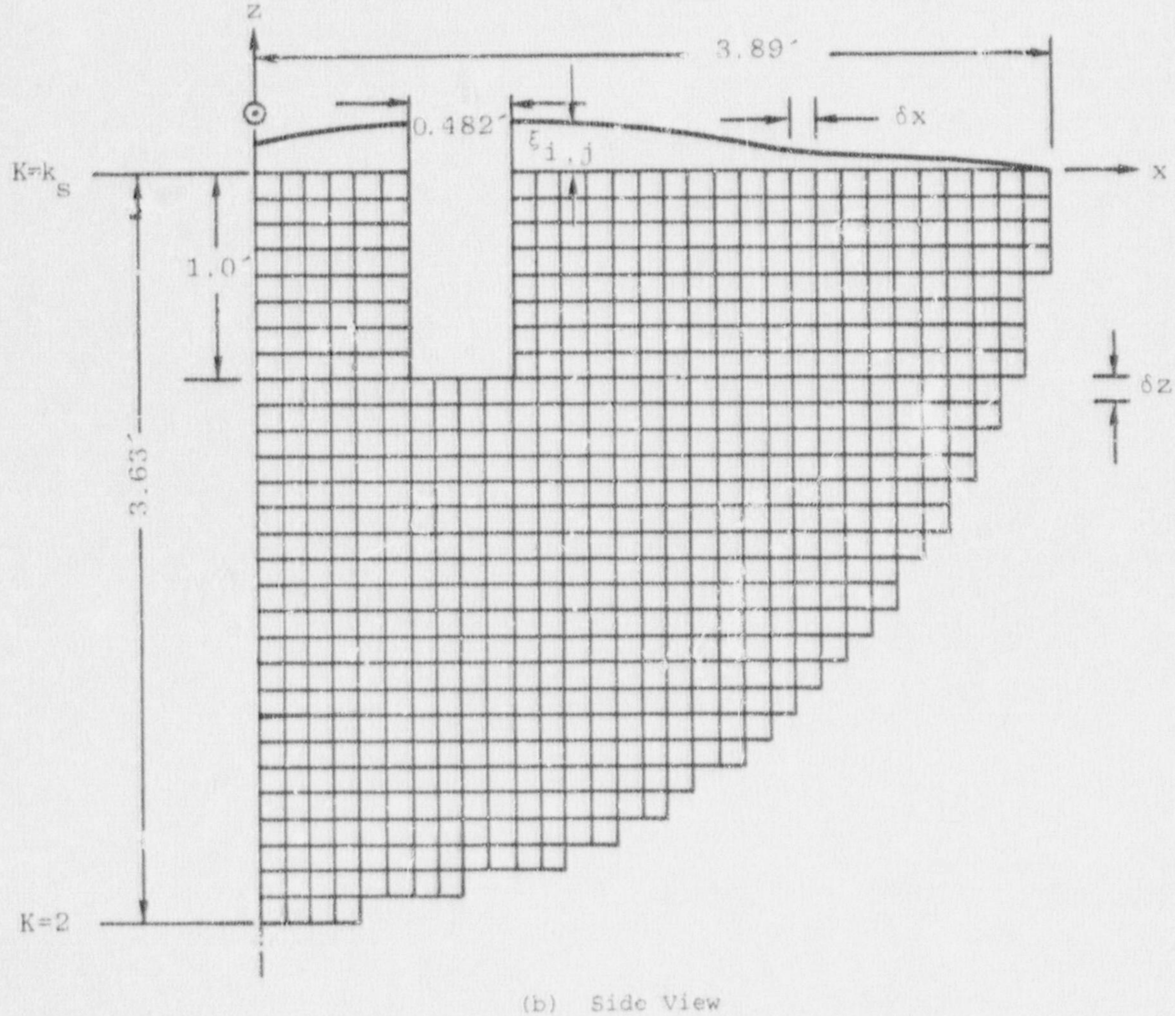

(b) Side View

Figure 2.5. Mesh Configuration for SWELL3 Simulations

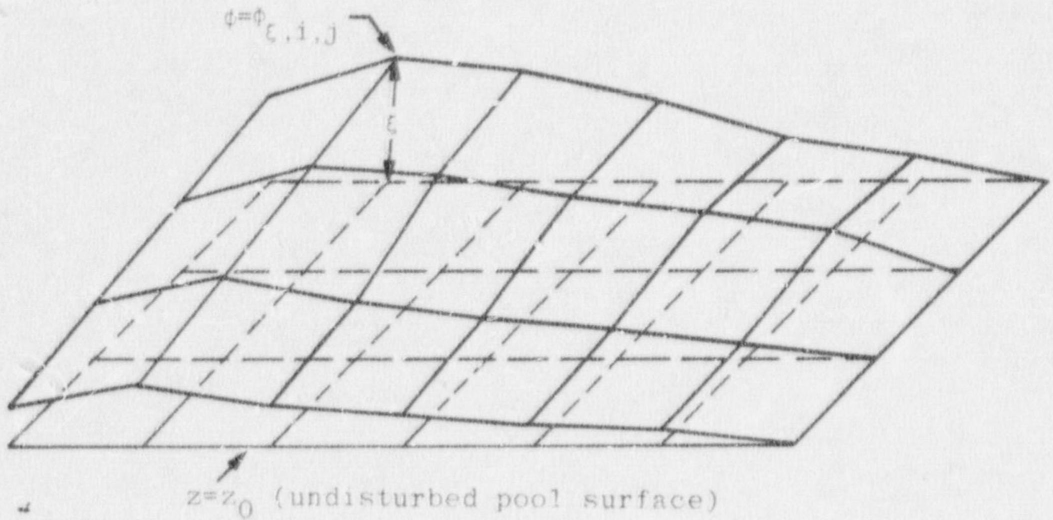

Figure 2.6. Pool Surface Perspective

$$R = \begin{bmatrix} x = x(\alpha,\beta) \\ y = y(\alpha,\beta) \\ z = z(\alpha,\beta) \end{bmatrix} \quad (0 \le \alpha \le 1;\ 0 \le \beta \le 1)$$

so that on the surface R the velocity potential is

$$\phi_R(\alpha,\beta) = \phi[x(\alpha,\beta),\ y(\alpha,\beta),\ z(\alpha,\beta)] \quad .$$

Numerically this is accomplished by covering the surface with triangles as shown in Figure 2.7 for the initial flat surface at the end of the downcomer and in Figure 2.8 for the bubble surface at a later time. On the computer this is done by keeping two lists: a list of vertices,

$$R(p) = (x_p, y_p, z_p), \quad 1 \le p \le m \ ,$$

where

$$\phi_p = \phi[R(p)]$$

and a list of triangles

$$T(q) = (p_{1,q}, p_{2,q}, p_{3,q}), \quad 1 \le q \le n \quad ,$$

so that the coordinates of vertex ℓ, (ℓ = 1, 2, or 3) of triangle q is $R(p_{\ell,q})$.

As indicated in Figure 2.9, no computations are performed and no variables are defined at mesh points which are inside the bubble. Let

$$\left.\begin{aligned} \Delta x_{i+\frac{1}{2}} &= x_{i+1} - x_i \\ \Delta y_{j+\frac{1}{2}} &= y_{j+1} - y_j \\ \Delta z_{k+\frac{1}{2}} &= z_{k+1} - z_k \quad . \end{aligned}\right\} \qquad (2\text{-}23)$$

Then, at an interior mesh point (i,j,k) whose six cell neighbors are also within the fluid, the finite difference approximation to the Laplace equation (2-18), in Cartesian coordinates, is

$$\frac{1}{\Delta x_i}\left[\frac{\phi_{i+1,j,k} - \phi_{i,j,k}}{\Delta x_{i+\frac{1}{2}}} - \frac{\phi_{i,j,k} - \phi_{i-1,j,k}}{\Delta x_{i-\frac{1}{2}}}\right]$$

$$+ \frac{1}{\Delta y_j}\left[\frac{\phi_{i,j+1,k} - \phi_{i,j,k}}{\Delta y_{j+\frac{1}{2}}} - \frac{\phi_{i,j,k} - \phi_{i,j-1,k}}{\Delta y_{j-\frac{1}{2}}}\right]$$

$$+ \frac{1}{\Delta z_k}\left[\frac{\phi_{i,j,k+1} - \phi_{i,j,k}}{\Delta z_{k+\frac{1}{2}}} - \frac{\phi_{i,j,k} - \phi_{i,j,k-1}}{\Delta z_{k-\frac{1}{2}}}\right] = 0 \quad . \qquad (2\text{-}24)$$

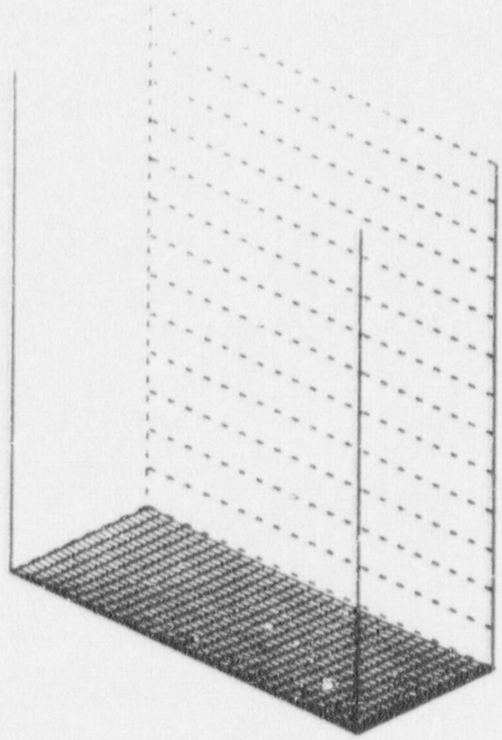

Figure 2.7. Initial Bubble Surface at Exit of Downcomer (The plane of symmetry is covered with broken lines. The diagonals that define the triangles are not shown here. See Figure 2.13 for the diagonals.)

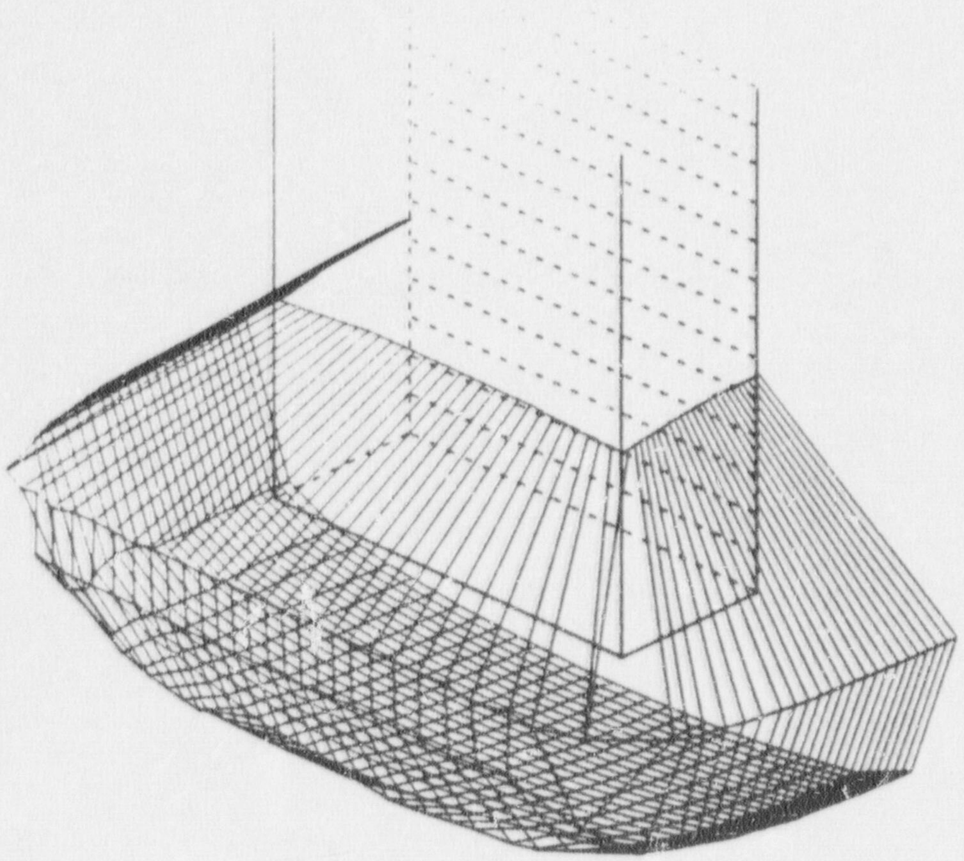

Figure 2.8. Bubble at Exit of Downcomer

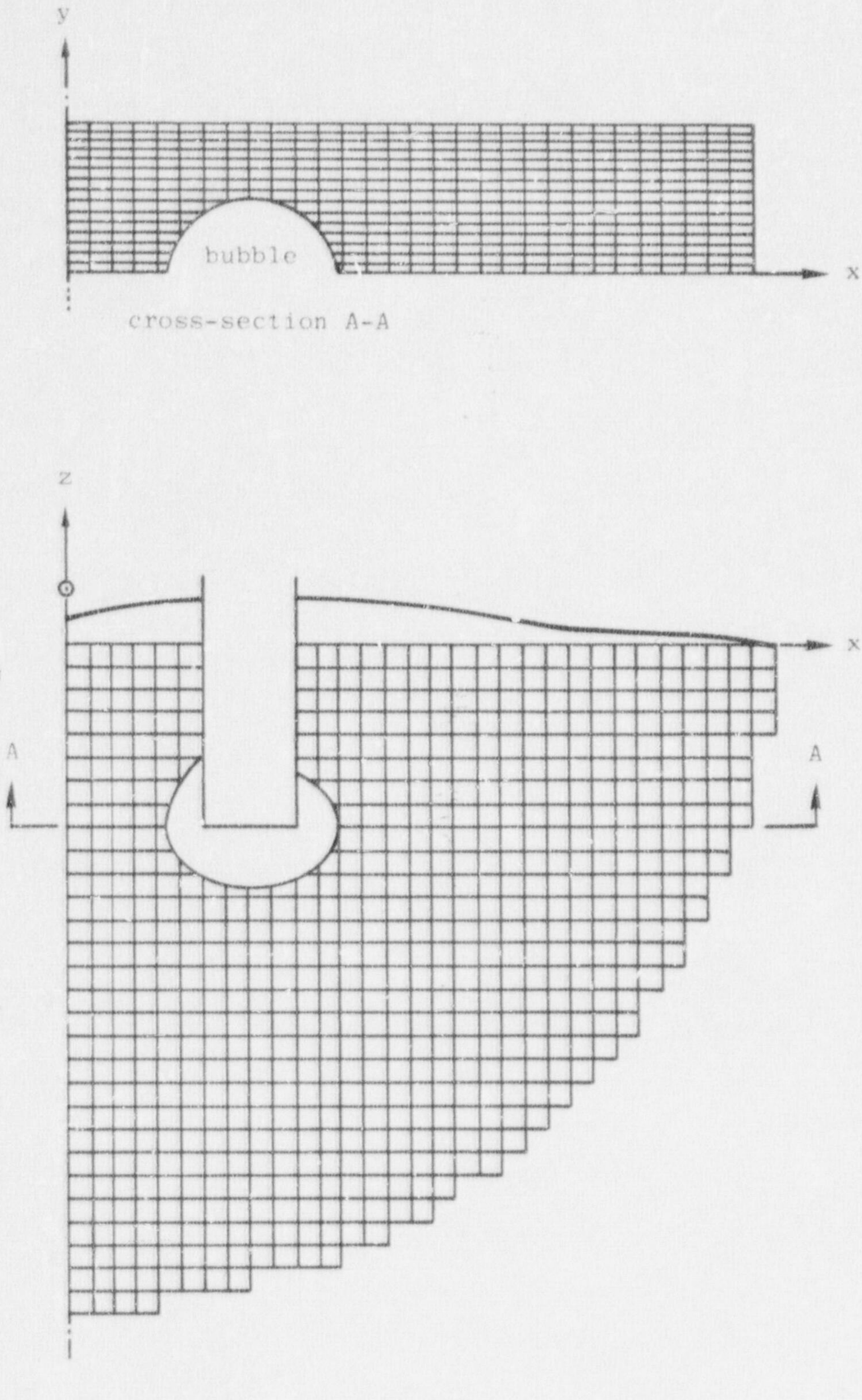

Figure 2.9. Cross-Sections of Finite Difference Mesh
Showing Bubble Surface

where

$$\Delta x_i = \frac{1}{2}(\Delta x_{i+\frac{1}{2}} + \Delta x_{i-\frac{1}{2}})$$

$$\Delta y_j = \frac{1}{2}(\Delta y_{j+\frac{1}{2}} + \Delta y_{j-\frac{1}{2}})$$

$$\Delta z_k = \frac{1}{2}(\Delta z_{k+\frac{1}{2}} + \Delta z_{k-\frac{1}{2}}) \quad . \tag{2-25}$$

If one or more of the six neighbors of the interior point (i,j,k) are outside the fluid region, i.e., inside the bubble, then the irregular star procedure is used to approximate Equation (2-18). For example, if $(i,j,k+1)$ lies outside the fluid, as shown in Figure 2.10, let δz be the distance from point (i,j,k) to the free surface along the mesh line connecting point (i,j,k) to point $(i,j,k+1)$ and ϕ_s be the value of the potential at this intersection point. The irregular star equation for the potential at (i,j,k) is then obtained by substituting δz for $\Delta z_{k+\frac{1}{2}}$ and ϕ_s for $\phi_{i,j,k+1}$ in Equations (2-24) and (2-25). Figure 2.11 depicts an irregular star in three dimensions about a point (i,j,k). The three points $(i+1,j,k)$, $(i,j+1,k)$ and $(i,j,k+1)$ in Figure 2.11 are all outside the fluid domain. The "regular legs" have lengths of the mesh sizes, Δx, Δy, and Δz, while the shorter "irregular legs" are labeled δx, δy, and δz.

For points which lie on rigid boundaries parallel to one of the coordinate planes, the normal derivative boundary condition Equation (2-19) is combined with the discrete form of the Laplace Equation (2-24) to obtain an equation for the potential on the boundary. For example, at the plane of symmetry $x = 0$, Equation (2-19) becomes

$$\frac{\partial \phi}{\partial x} = 0$$

which we approximate by

$$\frac{\phi_{i+1,j,k} - \phi_{i-1,j,k}}{\Delta x_{i+\frac{1}{2}} + \Delta x_{i-\frac{1}{2}}} = 0 \quad .$$

Observe that in this case the point $(i-1,j,k)$ is outside the fluid region, i.e., it is a "fictitious point." The desired equation at the plane of symmetry is obtained by substituting

$$\phi_{i-1,j,k} = \phi_{i+1,j,k} \tag{2-27}$$

into Equation (2-24) so that fictitious cells are not used in the calculations.

Special problems arise with edges or corners. There are two kinds of edges (or corners): concave as on the edge defined by the intersection of the two symmetry

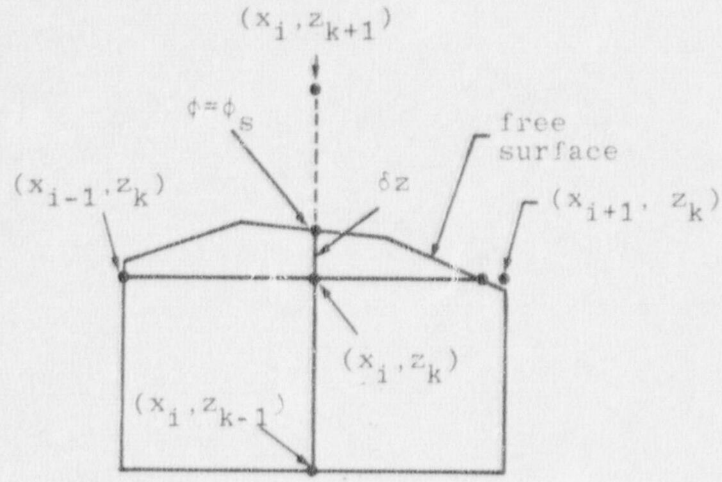

Figure 2.10. Irregular Star in a Two-Dimensional Space

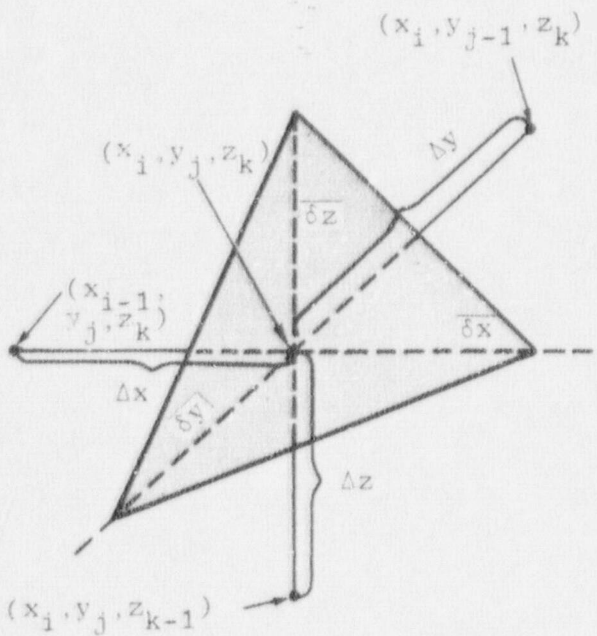

Figure 2.11. Three-Dimensional Irregular Star

planes x = 0 and y = 0, and convex as on the protruding edges of the rectangular downcomer. On the concave edge both the conditions $\frac{\partial\phi}{\partial x} = 0$ and $\frac{\partial\phi}{\partial y} = 0$ are applied as in the preceding paragraph. At the convex edges, however, each of the six neighbors of an edge point lies within the fluid; hence at these convex edge points Equation (2-24) is used without modification.

On the surface of the torus wall the boundary condition Equation (2-19) can be written

$$\frac{\partial\phi}{\partial x}\cos\beta - \frac{\partial\phi}{\partial z}\sin\beta = 0 \qquad (2\text{-}28)$$

where, as shown in Figure 2.4, β is the angle between the x-axis and the line normal to the torus. At points on the step-like surface shown in Figure 2.5 which approximates the torus surface, the finite difference expression used for Equation (2-28) is

$$\left(\frac{\phi_{i,j,k} - \phi_{i-1,j,k}}{\Delta x_{i-\frac{1}{2}}}\right)\cos\beta - \left(\frac{\phi_{i,j,k+1} - \phi_{i,j,k}}{\Delta z_{k+\frac{1}{2}}}\right)\sin\beta = 0 \quad . \qquad (2\text{-}29)$$

At the instant of vent clearing a switch is made from the vent clearing model to the bubble formation model. The initial values of ϕ in the pool for the bubble formation calculation are given by Equation (2-9). For problems with "full Δp" condition; i.e., at the time of drywell pressurization the pressure differential Δp between the wetwell airspace and the drywell is such that the initial water surface in the downcomer is at its exit, the vent clearing model is not needed and the initial condition is simply $\phi \equiv 0$ everywhere. In either case a surface composed of triangles, as shown in Figure 2.7, is placed at the exit of the downcomer. Within a rectangular finite difference cell the potential is assumed to vary linearly along lines parallel to the spatial axes so that the potential ϕ_p at a bubble surface point $R_p = (x_p, y_p, z_p)$, which is located within a cell, is given by

$$\phi_p = \sum_{\alpha=0}^{1} \sum_{\beta=0}^{1} \sum_{\gamma=0}^{1} a_{\alpha,\beta,\gamma}\, x_p^{\alpha}\, y_p^{\beta}\, z_p^{\gamma} \qquad (2\text{-}30)$$

where the eight coefficients $a_{\alpha,\beta,\gamma}$ are determined by the values of the potential at the eight corners of the cell. Also, at vent clearing the value of the pool surface displacement is assumed to be

$$\xi_{i,j} = 0 \quad , \tag{2-31}$$

and the potential at $\xi_{i,j}$ is

$$\phi_{\xi,i,j} = 0 \quad . \tag{2-32}$$

On the bubble surface, an explicit finite difference procedure is used to advance the values of the free surface potential and positions. A bubble surface point is moved from its old position R_p^n to the new position R_p^{n+1} by

$$R_p^{n+1} = R_p^n + U_p^n \, \Delta t^n \tag{2-33}$$

where the superscript n refers to the time t and n+1 to the new time level $t + \Delta t^n$.

Similarly, ϕ_p^{n+1} on the bubble surface is determined from the approximation

$$\phi_p^{n+1} = \phi_p^n + \Delta t^n \left\{ \frac{1}{2}\left[(u_p^n)^2 + (v_p^n)^2 + (w_p^n)^2\right] - \frac{p_{bub}^n - p_{air}^n}{\rho} - g\,(z_p^n - z_0) \right\} \tag{2-34}$$

to the Bernoulli equation, Equation (2-20). In the equation above the particle velocity $U_p^n = (u_p^n, v_p^n, w_p^n)$ at point R_p is determined by an extrapolation procedure to be described later in this section. The wetwell airspace pressure, p_{air}^n, at time t^n is determined from the airspace volume V_{air}^n by the adiabatic relationship

$$p_{air}^n = p_{air}^0 \left(\frac{V_{air}^0}{V_{air}^n} \right)^\gamma \tag{2-35}$$

where the specific heat ratio γ is taken as 1.4.

To avoid bunching up of the bubble points which lie on the sides of the downcomer (not those on the plane of symmetry), we constrain these points to move only in the vertical direction. For these bubble surface points, the discretization of the applicable form of the Bernoulli equation is

$$\phi_p^{n+1} = \phi_p^n + \Delta t^n \left\{ \frac{1}{2}\left[(w_p^n)^2 - (u_p^n)^2 - (v_p^n)^2\right] - \frac{p_{bub}^n - p_{air}^n}{\rho} - g(z_p^n - z_0) \right\} \tag{2-36}$$

On the pool surface, an implicit numerical procedure is used to advance the values of the pool surface displacement, ξ, and the pool surface potential, ϕ_ξ. For example, the pool surface displacement is advanced by

$$\xi^{n+1} = \xi^n + \frac{1}{2}\Delta t^n (w^n + w^{n+1}) \ . \tag{2-37}$$

This method is practical due to the simple representation of the pool surface, whereas, for the bubble surface such an implicit procedure is impractical since it would require the execution of the algorithm to form the irregular stars at each iteration. Let k_s denote the vertical cell index of the undisturbed pool surface, Figure 2.5(b), then the finite difference approximation to the governing equation (2-21) at a point (i,j) on the pool surface is the two-step procedure:

$$\phi^{n+\frac{1}{2}}_{\xi,i,j} = \phi^n_{\xi,i,j} + \frac{1}{2}\Delta t^n \left\{ \frac{1}{2}\left[(w^n_{\xi,i,j})^2 - (u^n_{i,j,k_s})^2 - (v^n_{i,j,k_s})^2 \right] - g\,\xi^n_{i,j} \right\} \tag{2-38a}$$

$$\phi^{n+1}_{\xi,i,j} = \phi^{n+\frac{1}{2}}_{\xi,i,j} + \frac{1}{2}\Delta t^n \left\{ \frac{1}{2}\left[(w^{n+1}_{\xi,i,j})^2 - (u^{n+1}_{i,j,k_s})^2 - (v^{n+1}_{i,j,k_s})^2 \right] - g\,\xi^{n+1}_{i,j} \right\} \ . \tag{2-38b}$$

Equation (2-37) can also be represented by a two-step operation:

$$\xi^{n+\frac{1}{2}}_{i,j} = \xi^n_{i,j} + \frac{1}{2}\Delta t^n\, w^n_{\xi,i,j} \tag{2-39a}$$

$$\xi^{n+1}_{i,j} = \xi^{n+\frac{1}{2}}_{i,j} + \frac{1}{2}\Delta t^n\, w^{n+1}_{\xi,i,j} \tag{2-39b}$$

where

$$w^n_{\xi,i,j} = (\phi^n_{\xi,i,j} - \phi^n_{i,j,k_s-1})/(\xi^n_{i,j} + \Delta z_{k_s-\frac{1}{2}})$$

$$u^n_{i,j,k} = (\phi^n_{i+1,j,k} - \phi^n_{i-1,j,k})/(2\ \Delta x_i)$$

$$v^n_{i,j,k} = (\phi^n_{i,j+1,k} - \phi^n_{i,j-1,k})/(2\ \Delta y_j)$$

$$w^n_{i,j,k} = (\phi^n_{i,j,k+1} - \phi^n_{i,j,k-1})/(2\ \Delta z_k) \ . \tag{2-40}$$

At the position of the undisturbed free surface, $k = k_s$, we assume the potential varies linearly between the point $z = z_{i,j,k_s-1}$ and the point $z = z_0+\xi_{i,j}$ so that

$$\phi^n_{i,j,k_s} = \frac{(\xi^n_{i,j}\,\phi_{i,j,k_s-1} + \Delta z_{k_s-\frac{1}{2}}\,\phi_{\xi,i,j})}{\xi^n_{i,j} + \Delta z_{k_s-\frac{1}{2}}} \quad . \tag{2-41}$$

To advance the solution from ϕ^n to ϕ^{n+1}, first explicitly advance the bubble surface position and potential, using Equations (2-33), (2-34), (2-36), (2-38a), and (2-39a). Then solve the system of linear algebraic equations given by Equations (2-24), (2-29), (2-41), and the modifications of Equation (2-24) due to rigid body boundary conditions and irregular stars. In this second step Equation (2-39b) and the nonlinear Equation (2-38b) are also used. This system of algebraic equations is solved by an SOR procedure as given in Appendix A1.

Velocity Calculation

The velocity U at a point in the fluid is given from Equation (2-17) as

$$U = \left(\frac{\partial\phi}{\partial x}, \frac{\partial\phi}{\partial y}, \frac{\partial\phi}{\partial z}\right) \quad .$$

At interior grid points and on rigid boundaries parallel to coordinate planes, the components of U are simply calculated by the centered difference equations, Equation (2-40). At grid points on the torus wall, we use one-sided finite difference approximations to obtain

$$u_{i,j,k} = \frac{\phi_{i,j,k} - \phi_{i-1,j,k}}{\Delta x_{i-\frac{1}{2}}}$$

$$w_{i,j,k} = \frac{\phi_{i,j,k+1} - \phi_{i,j,k}}{\Delta z_{k+\frac{1}{2}}} \tag{2-42}$$

for u and w. The standard centered difference form in Equation (2-40) is used for transverse component v at the torus wall.

A more difficult and numerically more sensitive problem is to find a satisfactory approximation to the gradient of the potential at points on the bubble surface. The evaluation of velocities on the bubble surface is important since they can provide a large contribution to the discretized Bernoulli equation (2-34). This equation, through the velocity and the pressure differential between the bubble and pool surface, drives the entire solution. At each time level it provides boundary values of ϕ for the Laplace equation. Hence, to obtain a satisfactory solution of ϕ, the velocity field on the bubble surface must be relatively smooth both spatially and temporally. For the sake of simplicity we describe the procedure which is used to calculate these velocities in two spatial dimensions instead of three. To find the velocity at point p_s on the surface of the bubble shown in Figure 2.12, first find two interior points p_1 and p_2 on the line "normal" to the surface at p_s such that the points p_1 and p_2 possess the following properties:

(1) p_1 and p_2 are not both in the same rectangular cell.

(2) The distance between p_1 and p_2 is at least the width of a cell.

(3) All corners of the cells containing p_1 and p_2 are in the fluid interior.

(4) p_1 and p_2 are as close to p_s as possible with regards to (1), (2), and (3).

Then under the restrictions above, we can find the velocity at the corners of the cells containing p_1 and p_2 and, hence, find each component of velocity at both p_1 and p_2, using linearity as in Equation (2-30). The velocity at p_s is then found from the velocities at p_1 and p_2 by linear extrapolations. The normal to the bubble surface at p_s is defined as the direction normal to the line connecting the two (in two-dimensional case) adjacent surface points on either side of p_s. In three dimensions, we use the direction of the normal to the plane determined by the three adjacent points (a, b, and c in Figure 2.13) which surround the point p_s.

Pressure, Load, and Impulse on Torus

After obtaining the solution of the finite difference equations for the bubble formation model, we have a record of the potential $\phi^n_{i,j,k}$ at points on and within the fluid at the discrete times t^n encompassed by the calculation. Specifically, we have the time history of the potential on the surface of the torus. From this we can use the Bernoulli equation, Equation (2-22), to find the pressure p and hence the load given by

$$L = (\ell_x, \ell_y, \ell_z) = \int_{torus} p\, N\, ds \ , \qquad (2\text{-}43)$$

where N is the unit vector normal to the torus wall.

The dynamic vertical load $\tilde{\ell}_z$ is defined as

$$\tilde{\ell}_z = \ell_z - [\text{weight of water}] \ ,$$

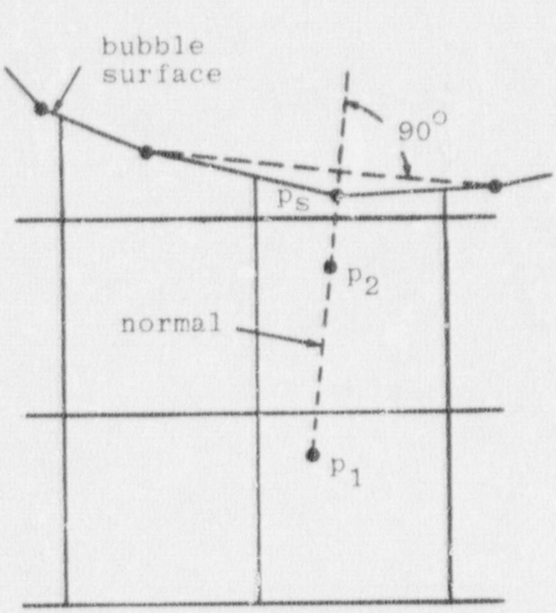

Figure 2.12. Velocity Extrapolation in a Two-Dimensional Space

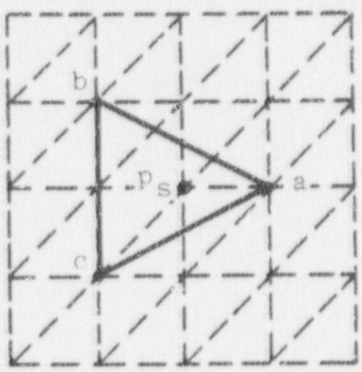

Figure 2.13. Surface Points Used to Determine the Normal at p_s.

or

$$\tilde{\ell}_z = \int_{\substack{\text{wetted}\\ \text{surface}\\ \text{of torus}}} \left\{ p - \left[p_{air} - \rho\, g\, (z - z_0) \right] \right\} dx\, dy \quad . \tag{2-44}$$

Solving for p in Equation (2-22) and substituting the result into Equation (2-44) we obtain

$$\tilde{\ell}_z = - \int_{\substack{\text{wetted}\\ \text{surface}\\ \text{of torus}}} \rho \left[\frac{\partial \phi}{\partial t} + \frac{1}{2}(u^2 + v^2 + w^2) \right] dx\, dy \quad . \tag{2-45}$$

Due to the geometric symmetry of the problem, the longitudinal and transverse components, ℓ_x and ℓ_y, respectively, of the load vanish. The impulse, I, is

$$I(t) = \int_0^t \tilde{\ell}_z\, (\tau)\, d\tau \quad . \tag{2-46}$$

Upon substituting Equation (2-45) into Equation (2-46) we obtain

$$I(t) = - \int_{\substack{\text{wetted}\\ \text{surface}}} \rho \left[\phi(t) + \frac{1}{2} \int_0^t (u^2 + v^2 + w^2)\, d\tau \right] dx\, dy \tag{2-47}$$

Instead of using Equation (2-45), the dynamic vertical load can be calculated by the inverse of Equation (2-46); i.e.,

$$\tilde{\ell}_z(t) = \frac{d}{dt} I(t) \quad . \tag{2-48}$$

From Equation (2-22) we calculate the pressure at a point (i,j,k) within the fluid by

$$p^n_{i,j,k} = p^n_{air} - \rho \left\{ g(z_k - z_0) + \frac{\phi^{n+1}_{i,j,k} - \phi^{n-1}_{i,j,k}}{\Delta t^{n-1} + \Delta t^n} + \lambda^n_{i,j,k} \right\} \tag{2-49}$$

where $\lambda \equiv \frac{1}{2}(u^2 + v^2 + w^2)$. The impulse is calculated by

$$I^n = - \rho \sum_{(i,j,k)\in\Gamma} \phi^n_{i,j,k}\, \Delta x_i\, \Delta y_j - \rho \sum_{\eta=1}^{n} \left[\sum_{(i,j,k)\in\Gamma} \lambda_{i,j,k}\, \Delta x_i\, \Delta y_j \right] \Delta t^{\eta-1} \tag{2-50}$$

where Γ is the set of points on the wall of the torus, and the dynamic vertical load is

$$\ell_z^n = \frac{I^{n+1} - I^{n-1}}{\Delta t^{n-1} + \Delta t^n} \quad . \tag{2-51}$$

In the bubble formation part of the SWELL3 model, Equations (2-49) to (2-51) are used to compute the pressure at selected points and to obtain the impulse and load on the torus wall. In the vent clearing part of the model, we use Equations (2-9) and (2-15) to obtain slightly different formulas for the same purpose:

$$p_{i,j,k}^n = p_{air} - \rho \left[g(z_k - z_0) - \left(\frac{dw}{dt}\right)^n \phi_{i,j,k}^* \right.$$
$$\left. + (w^n)^2 \lambda_{i,j,k}^* \right] \tag{2-52}$$

$$I^n = \rho w^n \sum_\Gamma \phi_{i,j,k}^* \Delta x_i \Delta y_j$$
$$- \rho \delta t \left[\sum_{\eta=1}^{n} (w^n)^2 \right] \left[\sum_\Gamma \lambda_{i,j,k}^* \Delta x_i \Delta y_j \right] \tag{2-53}$$

where $\lambda^* \equiv \frac{1}{2}\left[(\partial\phi^*/\partial x)^2 + (\partial\phi^*/\partial y)^2 + (\partial\phi^*/\partial z)^2\right]$. The dynamic vertical load ℓ_z^n is still given by Equation (2-51).

2.4 SWELL3 MODEL SUMMARY

The SWELL3 computer program incorporates a numerical method for calculating three-dimensional, incompressible, irrotational fluid flow in the presence of solid bodies and with multiple free surfaces. The method is applied to find the forces on a MARK I reactor containment design during the early stages of a postulated LOCA. The main features of the method are the use of three-dimensional irregular stars to form the Laplacian operator and the imposition of the fully nonlinear Bernoulli equation on free surfaces which are not restricted in their orientation. The major challenge inherent in this approach is the formation of the irregular star and the computation of velocities at points on free surfaces. The concepts of structured programming, linked lists, and free storage [4] were invaluable aids in programming the solution of this problem.

The following flow chart summarizes the solution procedure.

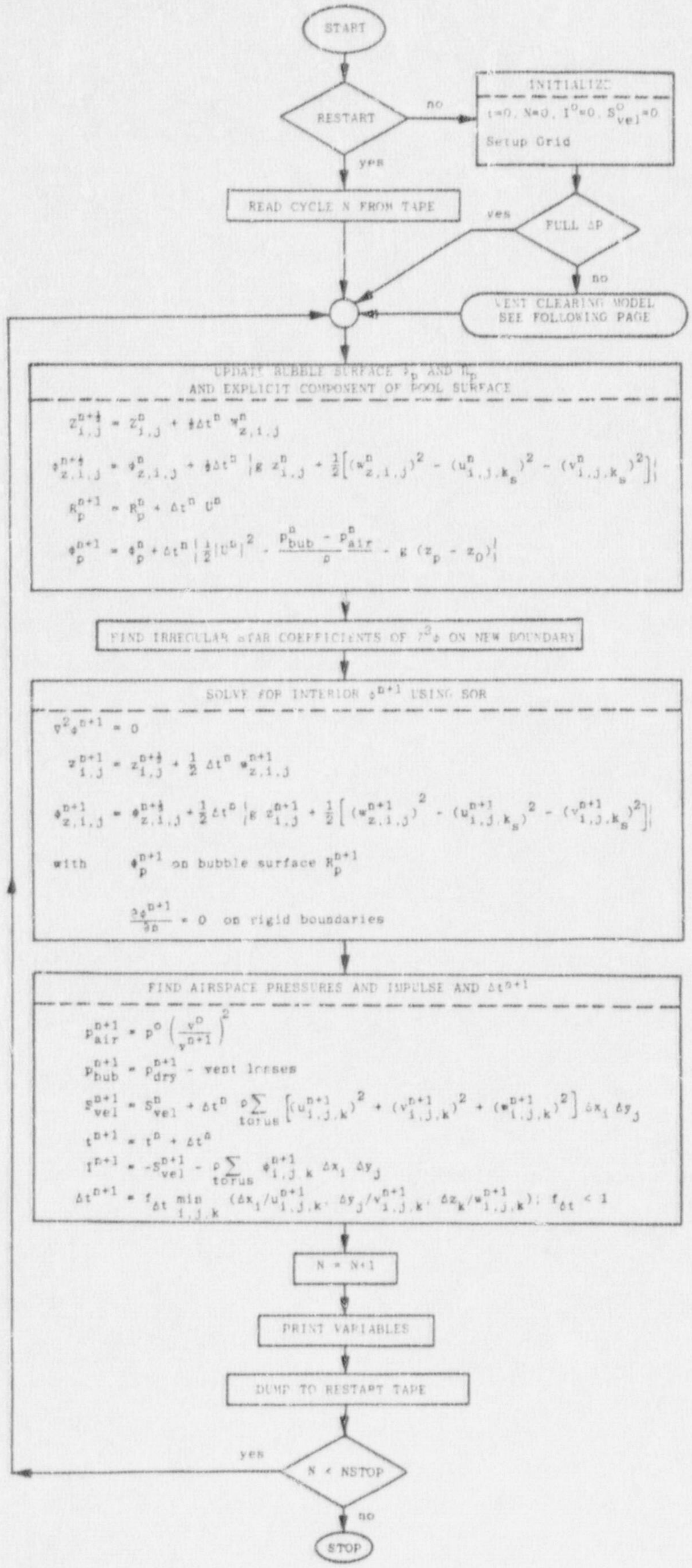
START
RESTART
no
yes
INITIALIZE
Setup Grid
READ CYCLE N FROM TAPE
FULL ΔP
yes
no
VENT CLEARING MODEL
SEE FOLLOWING PAGE
AND EXPLICIT COMPONENT OF POOL SURFACE
SOLVE FOR INTERIOR USING SOR
with
on bubble surface
on rigid boundaries
FIND AIRSPACE PRESSURES AND IMPULSE AND
vent losses
N = N+1
PRINT VARIABLES
DUMP TO RESTART TAPE
yes
N < NSTOP
no
STOP

VENT CLEARING MODEL

↓

SOLVE FOR $\phi^*_{i,j,k}$

$\nabla^2\phi = 0$ in interior: (19)

with

$\frac{\partial\phi^*}{n} = 0$ on rigid boundary; (22) or (24)

$\phi^*_{i,j,k_s} = 0$ on pool surface

$\phi^*_{i,j,k_d} = \phi^*_{i,j,k_{d-1}} - \Delta z_{k_{d-\frac{1}{2}}}$ on exit of downcomer

↓

$$I^* = \rho \sum_{\substack{\text{torus}\\ \text{wall}}} \phi^*_{i,j,k}\, \Delta x_i\, \Delta y_j$$

$$S^*_{vel} = \rho \sum_{\substack{\text{torus}\\ \text{wall}}} \left[(u^*_{i,j,k})^2 + (v^*_{i,j,k})^2 + (w^*_{i,j,k})^2\right] \Delta x_i\, \Delta y_j$$

↓

VELOCITY AT DOWNCOMER EXIT

$$w^m = w^m + \delta t \left\{\frac{a}{1 - ah}\left[\frac{1 - f}{2} w^2 + g(h - h_0) + \frac{p_1 - p_{air}}{\rho}\right]\right\}^{m+\frac{1}{2}}$$

$$h^{m+1} = h^m + \delta t\, w^{m+\frac{1}{2}}$$

$$t^{m+1} = t^m + \delta t$$

$$\tilde{S}^{m+1}_{vel} = \tilde{S}^m_{vel} + \delta t (w^{m+1})^2 S^*_{vel}$$

$$\tilde{I}^{m+1} = -\tilde{S}^{m+1}_{vel} + w^{m+1} I^*$$

↓

INITIALIZATION FOR BUBBLE GROWTH

$I^o = \tilde{I}^m \qquad S^o_{vel} = \tilde{S}^m_{vel}$

$\phi^o_{i,j,k} = -w^m \phi^*_{i,j,k}$

↓

END

Section 3

SURGE—MODEL FOR TWO-DIMENSIONAL POOL SWELL

The flow field becomes practically two-dimensional in the late times of pool swell in a single-cell configuration in which the spacing of downcomer cells is not too large. In the present study we use SWELL3 to compute the flow until the diameter of bubble reaches about half the spacing of downcomer cells. It has been found by numerous calculations that at this point the flow in the pool becomes essentially two-dimensional. In order to increase efficiency and, more important, to achieve greater accuracy when impact on the ring header occurs, the calculation is continued by the SURGE code after this point.

The SURGE code is primarily based on the Generalized Arbitrary Lagrangian-Eulerian (GALE) method [5], which is a very useful tool for treating two-dimensional, time-dependent incompressible flows in which free surfaces are present. In what follows we shall describe briefly the GALE method and its application to the pool swell problem.

3.1 THE GALE METHOD

First, the fluid domain of interest is divided into a number of quadrilaterals or cells such that natural boundaries, e.g., free surfaces, coincide with the mesh lines. A typical mesh for pool swell calculations is shown in Figure 3.1(a). Only one half of the pool needs be considered. The mesh configuration in Figure 3.1(a) may be interpreted as a mapping into a rectangular region shown in Figure 3.1(b). The Lagrangian coordinates (a,b) correspond to the mesh lines. The vertices of the computational cells are designated by the (i,j) subscript system (Figure 3.2); associated with each vertex are its cartesian space coordinates (x_{ij}, y_{ij}) and velocity components (u_{ij}, v_{ij}).

A set of initial conditions on (x,y) and (u,v) at each vertex is needed to begin a calculation. To advance the flow field with respect to time, the vertices are moved to their new positions according to their instantaneous velocities through an increment in time δt:

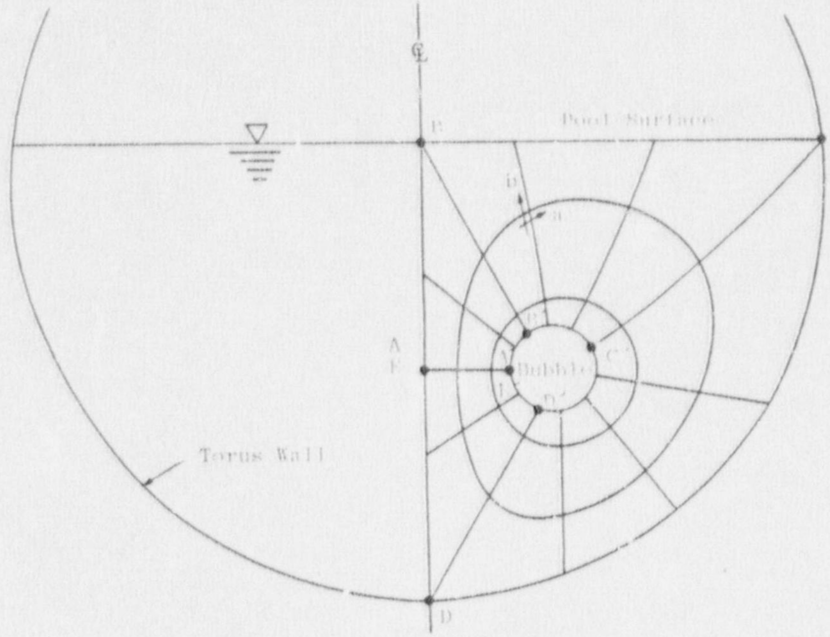

Figure 3.1(a). Schematic of the SURGE Mesh

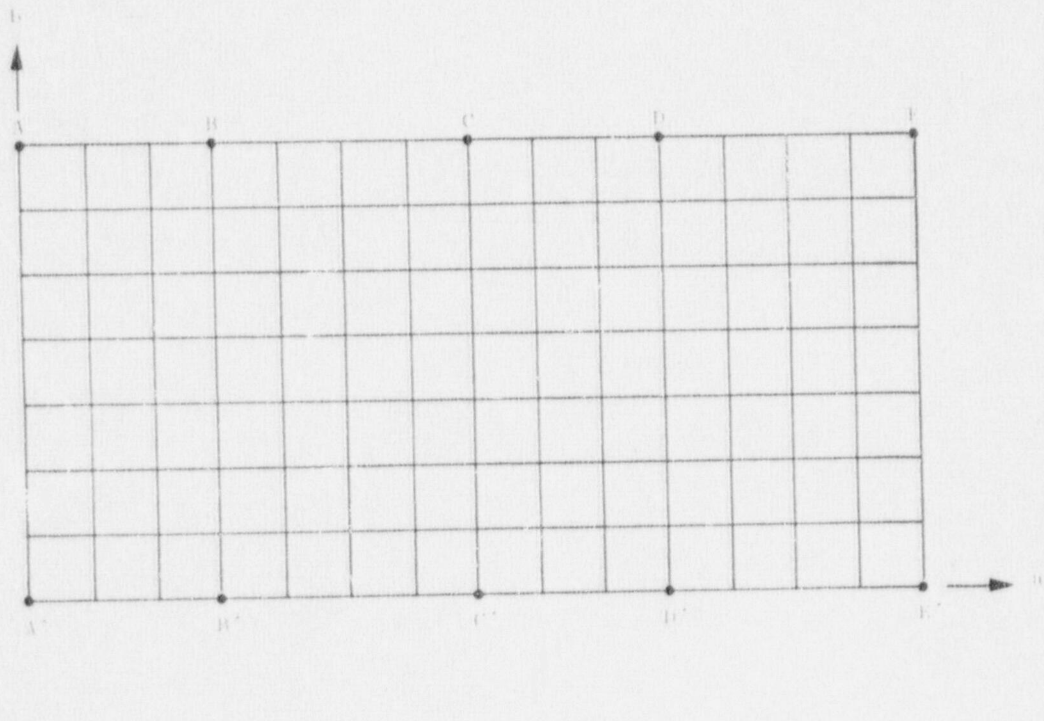

Figure 3.1(b). SURGE Mesh in the Lagrangian Space

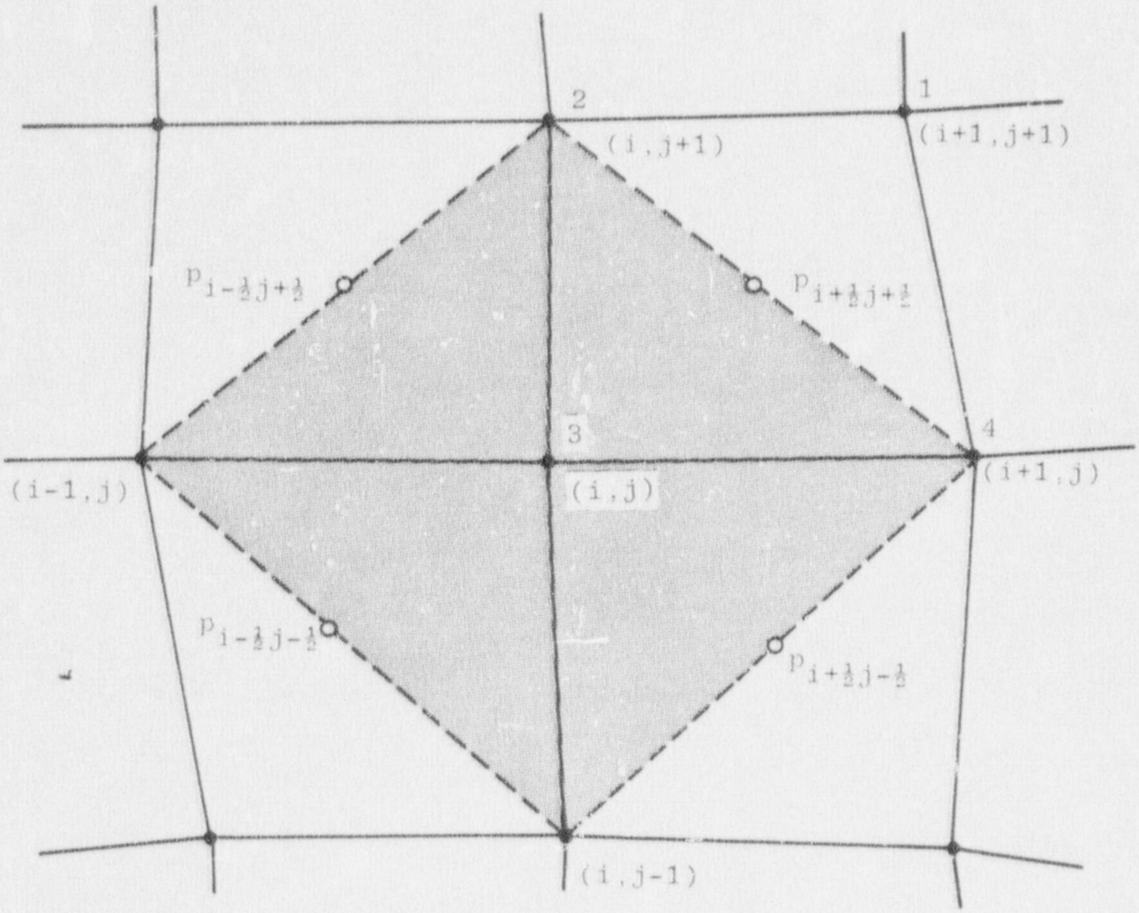

Figure 3.2. Control Volume for an Interior Vertex (i,j,)

$$\left.\begin{aligned} x_{ij}^{n+1} &= x_{ij}^{n} + \delta t\ u_{ij}^{n+1} \\ y_{ij}^{n+1} &= y_{ij}^{n} + \delta t\ v_{ij}^{n+1} \end{aligned}\right\} \qquad (3\text{-}1)$$

where the superscript n refers to the nth increment in time. Note that in Equation (3-1) the velocities (u,v) are evaluated at the new time level. Through this construction, appropriate boundary conditions can be satisfied at the new time level.

The velocities (u_{ij}^{n+1}, v_{ij}^{n+1}) are computed from the momentum equations. For the control volume of the vertex (i,j) in Figure 3.2, assuming (u_{ij}, v_{ij}) equal to the average velocities in the control volume, the discretized inviscid momentum equations can be written

$$\begin{aligned} \frac{u_{ij}^{n+1} - u_{ij}^{n}}{\delta t} = g_x + \frac{i}{M_{ij}} \Big[& P_{i-\frac{1}{2}j+\frac{1}{2}} (y_{ij+1}^{n} - y_{i-1j}^{n}) \\ & + P_{i-\frac{1}{2}j-\frac{1}{2}} (y_{i-1j}^{n} - y_{ij-1}^{n}) \\ & - P_{i+\frac{1}{2}j+\frac{1}{2}} (y_{ij+1}^{n} - y_{i+1j}^{n}) \\ & - P_{i+\frac{1}{2}j-\frac{1}{2}} (y_{i+1j}^{n} - j_{ij-1}^{n}) \Big] \end{aligned} \qquad (3\text{-}2)$$

$$\begin{aligned} \frac{v_{ij}^{n+1} - v_{ij}^{n}}{\delta t} = g_y + \frac{1}{M_{ij}} \Big[& P_{i+\frac{1}{2}j-\frac{1}{2}} (x_{i+1j}^{n} - x_{ij-1}^{n}) \\ & + P_{i-\frac{1}{2}j-\frac{1}{2}} (x_{ij-1}^{n} - x_{i-1j}^{n}) \\ & - P_{i+\frac{1}{2}j+\frac{1}{2}} (x_{i+1j}^{n} - x_{ij+1}^{n} \\ & - P_{i-\frac{1}{2}j+\frac{1}{2}} (x_{ij+1}^{n} - x_{i-1j}^{n}) \Big] \ . \end{aligned} \qquad (3\text{-}3)$$

For vertices lying on a boundary, such as the vertex (i,j) in Figure 3.3, the momentum equations are written as:

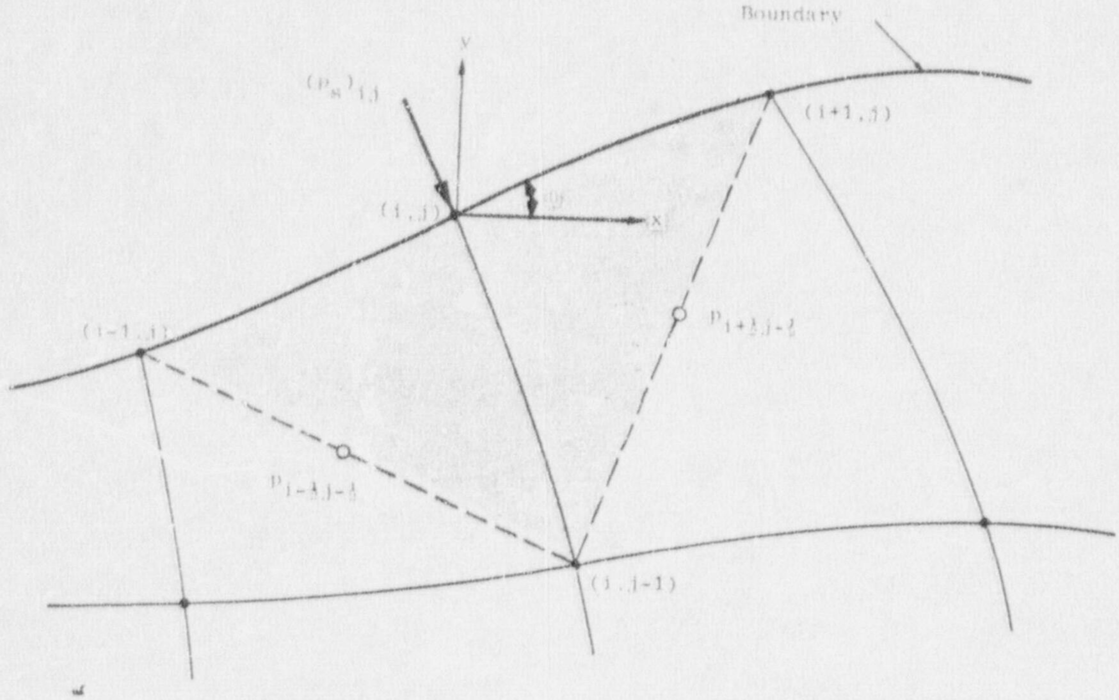

Figure 3.3. Control Volume for a Boundary Vertex

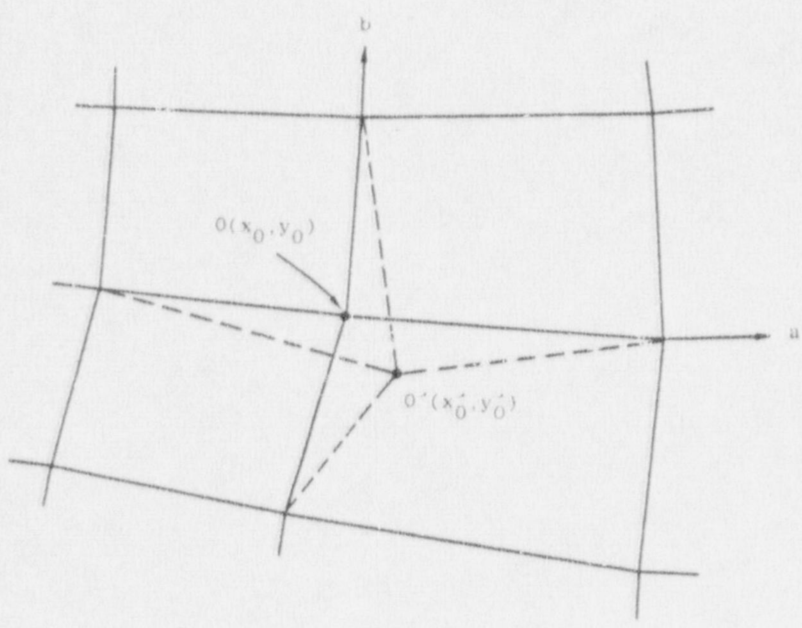

Figure 3.4. Illustration of the Rezoning Procedure

$$\frac{u^{n+1}_{ij} - v^{n}_{ij}}{\delta t} = g_x + \frac{1}{M_{ij}} \Big[(p_s)_{ij} \, (y^n_{i+1j} - y^n_{i-1j})$$

$$+ p_{i-\frac{1}{2}j-\frac{1}{2}} \, (y^n_{i-1j} - y^n_{ij-1})$$

$$- p_{i+\frac{1}{2}j-\frac{1}{2}} \, (y^n_{i+1j} - y^n_{ij-1}) \Big] \quad . \tag{3-4}$$

$$\frac{v^{n+1}_{ij} - v^{n}_{ij}}{\delta t} = g_y + \frac{1}{M_{ij}} \Big[p_{i+\frac{1}{2}j-\frac{1}{2}} \, (x^n_{i+1j} - x^n_{ij-1})$$

$$+ p_{i-\frac{1}{2}j-\frac{1}{2}} \, (x^n_{ij-1} - x^n_{i-1j})$$

$$- (p_s)_{ij} \, (x^n_{i+1j} - x^n_{i-1j}) \Big] \quad . \tag{3-5}$$

In the equation above, $p_{i+\frac{1}{2}j+\frac{1}{2}}$ is the average pressure defined at the center of each cell, (g_x, g_y) are the components of gravitational acceleration, M_{ij} is the mass of the control volume associated with the vertex (i,j) (the shaded areas in Figures 3.2 and 3.3), and $(p_s)_{ij}$ is the pressure acting on the boundary point. If the boundary is a free surface, $(p_s)_{ij}$ represents the instantaneous pressure exerting on the free surface and is a known quantity. If the boundary is one that separates the fluid from a rigid body, then p_s is to be determined from the iterative solution procedure, to be described shortly. It is clear that one must first obtain the pressure distribution before $(u^{n+1}_{ij}, v^{n+1}_{ij})$ can be calculated.

The pressure field is obtained by applying the principle of mass conservation. For an incompressible flow, such as water at speeds much lower than the speed of sound in the same medium, the fluid density can be regarded as constant and mass conservation means volume conservation. The volume of the cell $(i+\frac{1}{2}, j+\frac{1}{2})$ is

$$\tilde{V}^n_{i+\frac{1}{2}j+\frac{1}{2}} = \frac{1}{2}(x^n_{13} \, y^n_{24} - x^n_{24} \, y^n_{13}) \quad . \tag{3-6}$$

In most of this discussion, the subscripts 1, 2, 3, and 4 are abbreviations for the vertices of the cell $(i+\frac{1}{2}, j+\frac{1}{2})$ in Figure 3.2, and the notations $x^n_{13} \equiv x^n_1 - x^n_3$, $x^n_{24} \equiv x^n_2 - x^n_4$, etc., are used for convenience. For the new time level, we can write

$$\tilde{V}^{n+1}_{i+\frac{1}{2}j+\frac{1}{2}} = \frac{1}{2}(x^{n+1}_{13} \, y^{n+1}_{24} - x^{n+1}_{24} \, y^{n+1}_{13}) \quad . \tag{3-7}$$

Using Equations (3-1), (3-6), (3-7), and conservation of volume, i.e.,

$$\tilde{V}^{n+1}_{i+\frac{1}{2}j+\frac{1}{2}} = \tilde{V}^n_{i+\frac{1}{2}j+\frac{1}{2}} \, ,$$

we have

$$D_{i+\frac{1}{2}j+\frac{1}{2}} \equiv \bar{y}_{24}\, u_{13}^{n+1} - \bar{y}_{13}\, u_{24}^{n+1} - \bar{x}_{24}\, v_{13}^{n+1} + \bar{x}_{13}\, v_{24}^{n+1} = 0 \tag{3-8}$$

where

$$\left.\begin{aligned} \bar{x}_{13} &\equiv \frac{1}{2}(x_{13}^{n} + x_{13}^{n+1}) = x_{13}^{n} + \frac{\delta t}{2}\, u_{13}^{n+1} \\ \bar{x}_{24} &\equiv \frac{1}{2}(x_{24}^{n} + x_{24}^{n+1}) = x_{24}^{n} + \frac{\delta t}{2}\, u_{24}^{n+1} \end{aligned}\right\} \tag{3-9}$$

and similarly for $\bar{y}_{13}$ and $\bar{y}_{24}$.

One way to obtain the governing equation for pressure is to write momentum equations, similar to Equations (3-2) and (3-3), for all the four vertices of cell $(i+\frac{1}{2},\ j+\frac{1}{2})$. The resulting expressions for $(u,v)^{n+1}$ are then substituted into Equation (3-8). This operation will lead to an equation in which the unknown pressure $p_{i+\frac{1}{2}j+\frac{1}{2}}$ at the cell center is related to other unknown pressures in its immediate neighborhood. These unknown discrete values of pressure can be solved by successive over-relaxation.

From programming point of view, there is another method that is more attractive: The idea is to use an approximate pressure distribution, in Equations (3-2) and (3-3) for interior points and in Equations (3-4) and (3-5) for boundary points, to obtain provisional values for $(u,v)^{n+1}$ throughout the flow field. This provisional $(u,v)^{n+1}$ will not in general make $D_{i+\frac{1}{2}j+\frac{1}{2}}$ in Equation (3-8) vanish, nor will they satisfy boundary conditions. The next step is to make corrections on the pressure field so as to reduce the maximum value of $|D|$ in the flow and satisfy boundary conditions. To do so we need to known how much change in $D_{i+\frac{1}{2}j+\frac{1}{2}}$ is produced by a small change in $p_{i+\frac{1}{2}j+\frac{1}{2}}$. By applying Equations (3-2) and (3-3) at the four vertices 1, 2, 3, and 4 in Figure 3.2, it is easily found that to the first variation

$$\Delta u_1^{n+1} = +(\delta t\ \Delta p_{i+\frac{1}{2}j+\frac{1}{2}}\ y_{24}^{n})/M_1$$

$$\Delta u_3^{n+1} = -(\delta t\ \Delta p_{i+\frac{1}{2}j+\frac{1}{2}}\ y_{24}^{n})/M_3$$

$$\Delta u_2^{n+1} = -(\delta t\ \Delta p_{i+\frac{1}{2}j+\frac{1}{2}}\ y_{13}^{n})/M_2$$

$$\Delta u_4^{n+1} = +(\delta t\ \Delta p_{i+\frac{1}{2}j+\frac{1}{2}}\ y_{13}^{n})/M_4$$

$$\Delta v_1^{n+1} = -(\delta t\ \Delta p_{i+\frac{1}{2}j+\frac{1}{2}}\ x_{24}^n)/M_1$$

$$\Delta v_3^{n+1} = +(\delta t\ \Delta p_{i+\frac{1}{2}j+\frac{1}{2}}\ x_{24}^n)/M_3$$

$$\Delta v_2^{n+1} = +(\delta t\ \Delta p_{i+\frac{1}{2}j+\frac{1}{2}}\ x_{13}^n)/M_2$$

$$\Delta v_4^{n+1} = -(\delta t\ \Delta p_{i+\frac{1}{2}j+\frac{1}{2}}\ x_{13}^n)/M_4 \qquad (3\text{-}10)$$

where Δ means a small change. Similarly, by taking a first variation of the unknown quantities in Equation (3-8), we have

$$\Delta D_{i+\frac{1}{2}j+\frac{1}{2}} = \bar{y}_{24}\ (\Delta u_1^{n+1} - \Delta u_3^{n+1}) - \bar{y}_{13}\ (\Delta u_2^{n+1} - \Delta u_4^{n+1})$$

$$- \bar{x}_{24}\ (\Delta v_1^{n+1} - \Delta v_3^{n+1}) + \bar{x}_{13}\ (\Delta v_2^{n+1} - \Delta v_4^{n+1}) \qquad (3\text{-}11)$$

Now we can relate $\Delta D_{i+\frac{1}{2}j+\frac{1}{2}}$ to $\Delta p_{i+\frac{1}{2}j+\frac{1}{2}}$ by substituting Equations (3-10) into Equation (3-11), with the result

$$\Delta D_{i+\frac{1}{2}j+\frac{1}{2}} = \alpha\ \delta t\ \Delta p_{i+\frac{1}{2}j+\frac{1}{2}} \qquad (3\text{-}12)$$

where

$$\alpha = \left(\frac{1}{M_1} + \frac{1}{M_3}\right)(x_{24}^n\ \bar{x}_{24} + y_{24}^n\ \bar{y}_{24}) + \left(\frac{1}{M_2} + \frac{1}{M_4}\right)(x_{13}^n\ \bar{x}_{13} + y_{13}^n\ \bar{y}_{13})$$

Recall that our objective is to find the correction in pressure, $\Delta p_{i+\frac{1}{2}j+\frac{1}{2}}$, such that the subsequent corrections in $(u,v)^{n+1}$ will lead to diminishing values in $|D_{i+\frac{1}{2}j+\frac{1}{2}}|$. This can be accomplished by setting $\Delta D_{i+\frac{1}{2}j+\frac{1}{2}} = - D_{i+\frac{1}{2}j+\frac{1}{2}}$ in Equation (3-12) and obtaining

$$\Delta p_{i+\frac{1}{2}j+\frac{1}{2}} = - D_{i+\frac{1}{2}j+\frac{1}{2}}/(\alpha\ \delta t) \qquad (3\text{-}13)$$

which is the formula for computing the correction for the pressure at the center of each cell.

We also need a formula for correcting p_s, the pressure at a liquid-solid boundary. Assuming that the solid boundary has an angle of inclination θ at the vertex (i,j) as shown in Figure 3.3, then the boundary condition is

$$u_{ij}^{n+1} \sin\theta - v_{ij}^{n+1} \cos\theta = (V_N)_{ij}^{n+1} \qquad (3\text{-}14)$$

where $(V_N)_{ij}^{n+1}$ is the magnitude of the normal velocity of solid boundary. Equation (3-14) states that, normal to the wall, the fluid partical velocity equals that of the wall. Recall that $(u_{ij}^{n+1}, v_{ij}^{n+1})$ are calculated by the momentum Equations (3-4) and (3-5). We rewrite Equation (3-14) as

$$u_{ij}^{n+1} \sin\theta - v_{ij}^{n+1} \cos\theta - (V_N)_{ij}^{n+1} = (R_B)_{ij} \tag{3-15}$$

where $(R_B)_{ij}$ is the residual. Because provisional values of $(u_{ij}^{n+1}, v_{ij}^{n+1})$ are used, $(R_B)_{ij}$ does not vanish in general. The aim of iterative procedure is to correct $(p_s)_{ij}$ in Equations (3-4) and (3-5) successively so that $|(R_B)_{ij}|$ is reduced to an acceptable size. Taking first variation of Equations (3-4), (3-5), and (3-15), we obtain, respectively, the following relations.

$$\left.\begin{aligned} \Delta u_{ij}^{n+1} &= \frac{\delta t}{M_{ij}} (y_{i+1j}^n - y_{i-1j}^n)\, \Delta(p_s)_{ij} \\ \Delta v_{ij}^{n+1} &= -\frac{\delta t}{M_{ij}} (x_{i+1j}^n - x_{i-1j}^n)\, \Delta(p_s)_{ij} \end{aligned}\right\} \tag{3-16}$$

$$\Delta u_{ij}^{n+1} \sin\theta - \Delta v_{ij}^{n+1} \cos\theta = \Delta(R_B)_{ij} = -(R_B)_{ij} \tag{3-17}$$

In Equation (3-17), $\Delta(R_B)_{ij}$ is set equal to $-(R_B)_{ij}$, the intention being to drive $|(R_B)_{ij}|$ toward zero. Substituting Equations (3-16) into Equation (3-17), we obtain

$$\Delta(p_s) = -(R_B)_{ij}/\beta \tag{3-18}$$

where

$$\beta = \frac{\delta t}{M_{ij}} \left[(y_{i+1j}^n - y_{i-1j}^n) \sin\theta + (x_{i+1j}^n - x_{i-1j}^n) \cos\theta \right] \tag{3-19}$$

To summarize, the procedure for finding the pressure and velocity fields consists of two parts:

A. Predictor—An approximate pressure distribution, i.e., p_{ij} and p_s, is used in Equations (3-2) through (3-5) to calculate provisional $(u,v)^{n+1}$ throughout the mesh. For a time-dependent problem, the pressure field of a previous time level can be used as the first approximation to reduce the number of iterations in the corrector phase.

B. Corrector—Sweep the mesh systematically; i.e., visit the cells sequentially. When a particular cell $(i+\frac{1}{2},j+\frac{1}{2})$ is visited, first calculate $D_{i+\frac{1}{2}j+\frac{1}{2}}$ by Equation (3-8). Then, Equation (3-13) gives $\Delta p_{i+\frac{1}{2}j+\frac{1}{2}}$ which is the correction we have to add to $p_{i+\frac{1}{2}j+\frac{1}{2}}$. Let the superscript ν denote the iteration number, then

$$p_{i+\frac{1}{2}j+\frac{1}{2}}^{(\nu+1)} = p_{i+\frac{1}{2}j+\frac{1}{2}}^{(\nu)} + \Delta p_{i+\frac{1}{2}j+\frac{1}{2}} \tag{3-20}$$

After that, Equations (3-10) are used to calculate the changes in $(u,v)^{n+1}$ at the four vertices of cell $(i+\frac{1}{2},j+\frac{1}{2})$, that are caused by $\Delta p_{i+\frac{1}{2}j+\frac{1}{2}}$. Make corrections in $(u,v)^{n+1}$ by

$$(u_1^{n+1})^{(\nu+1)} = (u_1^{n+1})^{(\nu)} + \Delta u_1^{n+1} \tag{3-21}$$

and similarly for u_2^{n+1}, u_3^{n+1}, etc. After sweeping the interior cells, visit each vertex lying on a rigid boundary and calculate the residual $(R_B)_{ij}$ according to Equation (3-15). Then use Equation (3-18) to find the pressure correction $\Delta(p_s)_{ij}$, and Equations (3-16) give the corresponding corrections in the boundary velocities. The corrector is repeated until the maximum values of $|D_{i+\frac{1}{2}j+\frac{1}{2}}|$ and $|(R_B)_{ij}|$ become less than a prescribed level.

After obtaining the field of $(u,v)^{n+1}$, the position of vertices are changed by using Equations (3-1), and the integration of the flow field by one time increment is now completed. To maintain stability in numerical integration, the time step δt should be chosen such that no vertex moves more than the minimum mesh spacing during that period. This condition can be satisfied by

$$\delta t = \frac{1}{4} \sqrt{L^2} / \max \left\{ |u|, |v| \right\} \tag{3-22}$$

where

$$L^2 = \min |\tilde{V}| \quad ,$$

and $\tilde{V}$ is defined in Equation (3-6).

3.2 MESH GENERATION, REZONING, AND SMOOTHING

A procedure by Thompson, et al. [6], is employed in SURGE to generate the curvilinear mesh shown in Figure 3.1(a). The first step is to select pairs of (x,y) along the boundary, i.e., along $\overline{ABCDE}$ and along $\overline{A'B'C'D'E'}$ in Figure 3.2(b). Thus, (x,y) at boundary vertices are fixed, except those along AA′ and EE′ which are periodic boundaries. The coordinates of interior vertices are obtained by solving

$$\left.\begin{aligned} \alpha^* \left(\frac{\partial^2 x}{\partial_a^2}\right) + \beta^* \left(\frac{\partial^2 x}{\partial a \partial b}\right) + \gamma^* \left(\frac{\partial^2 x}{\partial_b^2}\right) = 0 \\ \alpha^* \left(\frac{\partial^2 y}{\partial_a^2}\right) + \beta^* \left(\frac{\partial^2 y}{\partial a \partial b}\right) + \gamma^* \left(\frac{\partial^2 y}{\partial_b^2}\right) = 0 \end{aligned}\right\} \tag{3-23}$$

where

$$\alpha^* = (\partial x/\partial b)^2 + (\partial y/\partial b)^2$$

$$\beta^* = -2\left(\frac{\partial x}{\partial a}\frac{\partial x}{\partial b} + \frac{\partial y}{\partial a}\frac{\partial y}{\partial b}\right)$$

$$\gamma^* = (\partial x/\partial a)^2 + (\partial y/\partial a)^2$$

and (a,b) are the Lagrangian coordinate lines shown in Figure 3.1(a). Using finite-difference representations

$$\left.\begin{aligned}
\frac{\partial x}{\partial a} &= (x_{i+1j} - x_{i-1j})/2 \\
\frac{\partial x}{\partial b} &= (x_{ij+1} - x_{ij-1})/2 \\
\frac{\partial^2 x}{\partial a^2} &= x_{i+1j} - 2x_{ij} + x_{i-1j} \\
\frac{\partial^2 x}{\partial b^2} &= x_{ij+1} - 2x_{ij} + x_{ij-1}
\end{aligned}\right\} \qquad (3\text{-}24)$$

and similarly for $(\partial y/\partial a)$, $(\partial y/\partial b)$, etc., in Equations (3-23), we obtain

$$\begin{aligned}
x_{ij} = \Big[&\alpha^*(x_{i+1j} + x_{i-1j}) + \gamma^*(x_{ij+1} + x_{ij-1}) \\
&+ \frac{\beta^*}{4}(x_{i+1j+1} - x_{i-1j+1} - x_{i+1j-1} \\
&+ x_{i-1j-1})\Big] \Big/ \Big[2(\alpha^* + \gamma^*)\Big]
\end{aligned}$$

$$\begin{aligned}
y_{ij} = \Big[&\alpha^*(y_{i+1j} + y_{i-1j}) + \gamma^*(y_{ij+1} + y_{ij-1}) \\
&+ \frac{\beta^*}{4}(y_{i+1j+1} - y_{i-1j+1} - y_{i+1j-1} \\
&+ y_{i-1j-1})\Big] \Big/ \Big[2(\alpha^* + \gamma^*)\Big] \qquad (3\text{-}25)
\end{aligned}$$

These are the formulas for solving for (x_{ij}, y_{ij}) by the method of successive over-relaxation. Note that in Equation (3-24), we chose $\Delta a = \Delta b = 1$ in the Lagrangian space.

The procedure outlined in Section 3.1 employs the Lagrangian description of fluid motion; i.e., the vertices move with the fluid particle velocities. Its main advantage lies in that material interfaces are properly maintained and the absence of computational instability associated with convection terms. Its disadvantage, however, is that the cells can be badly distorted or even inverted in highly strained motions. To circumvent this difficulty, an automatic rezoning procedure is included in SURGE. At the end of each time increment; i.e., after the vertices are moved to their new positions, the vertex positions are adjusted so that a nearly optimum shape is always maintained for each cell. The rezoning procedure is in complete analogy with the method of mesh generation as described above. The first step is to adjust position of vertices lying on boundaries of the fluid domain. Then the interior vertices are moved by successive over-relaxation, using Equations (3-25). Only about five iterations are needed for each time step, since exact satisfaction of Equations (3-25) is not required for generating a desirable mesh configuration. After making the adjustment, due consideration must be given to the fact that, while $(x,y)_{ij}^{n+1}$ now represent the adjusted vertex position, $(u,v)_{ij}^{n+1}$ are still associated with the position prior to the adjustment.

As shown in Figure 3.4, suppose that the vertex 0 is moved to a new location 0′ in the rezoning operation. The problem is to find the velocities (u_0', v_0') for the new vertex 0′. Let Q represent either u or v. Then, using Taylor's series expansion to the second order in the (a,b) plane,

$$Q_0' = Q_0 + (\delta a)(\partial Q/\partial a)_0 + (\delta b)(\partial Q/\partial b)_0 + \frac{1}{2}\Big[(\delta a)^2(\partial^2 Q/\partial a^2)_0 + 2(\delta a)(\delta b)(\partial^2 Q/\partial a\partial b)_0 + (\delta b)^2(\partial^2 Q/\partial b^2)_0\Big] \tag{3-26}$$

To evaluate δa and δb, we have the following relations

$$\delta a = \left(\frac{\partial a}{\partial x}\right)_0 (x_0' - x_0) + \left(\frac{\partial a}{\partial y}\right)_0 (y_0' - y_0) = \frac{1}{J_0}\left[\left(\frac{\partial y}{\partial b}\right)_0 (x_0' - x_0) - \left(\frac{\partial x}{\partial b}\right)_0 (y_0' - y_0)\right]$$

$$\delta b = \left(\frac{\partial b}{\partial x}\right)_0 (x_0' - x_0) + \left(\frac{\partial b}{\partial y}\right)_0 (y_0' - y_0) = \frac{1}{J_0}\left[-\left(\frac{\partial y}{\partial a}\right)_0 (x_0' - x_0) + \left(\frac{\partial x}{\partial a}\right)_0 (y_0' - y_0)\right] \tag{3-27}$$

where

$$J_0 = \left(\frac{\partial x}{\partial a}\right)_0 \left(\frac{\partial y}{\partial b}\right)_0 - \left(\frac{\partial x}{\partial b}\right)_0 \left(\frac{\partial y}{\partial a}\right)_0 \qquad (3\text{-}28)$$

Now, to calculate Q_0' from Equation (3-26), various derivatives with respect to a and b can be evaluated at point 0 by central difference.

The growth of "alternating errors" is an instability which GALE shares with its predecessors. The alternating errors are noises with wavelength equal to two cell spacings in the Lagrangian space. In SURGE, a technique is used which effectively eliminates the alternating errors but gives very little damping to the meaningful part of the solution. At a given timestep, after the iterative procedure for finding $(u,v)_{ij}^{n+1}$ is terminated, the vertex velocities are adjusted according to

$$\begin{aligned}(Q_{ij})_{\text{adjusted}} = Q_{ij} + \frac{\lambda}{16} \Big[& 2(Q_{i+1j} + Q_{i-1j} + Q_{ij+1} + Q_{ij-1}) \\ & - Q_{i+1j+1} - Q_{i+1j-1} - Q_{i-1j+1} - Q_{i-1j-1} \\ & - 4\, Q_{ij} \Big] \end{aligned} \qquad (3\text{-}29)$$

where $Q = u$ or v. The damping parameter λ lies in the range $0 \leq \lambda \leq 1$. No damping takes place when $\lambda = 0$, and at $\lambda = 1$ all alternating errors are damped out in one timestep. Experience indicates that $\lambda = 0.2$ produces excellent results.

3.3 TRANSITION FROM SWELL3 TO SURGE

By observation it is found that the flow field becomes essentially two-dimensional during a SWELL3 calculation, when the bubble diameter reaches about 50% of the cell depth (spacing between downcomer pairs). At this point the transition is made from SWELL3 to SURGE. The flow field data to be transferred are the bubble volume, its time rate of change, the location of the bubble center, the velocity distribution (i.e., the average in the direction normal to the two-dimensional plane) along the pool surface, and the pool surface profile.

The first step is to create a SURGE mesh. It should be noted that the presence of downcomer pipes is ignored in SURGE. The mesh generation procedure, described in the preceding section, can be used here. The values of (x,y) for vertices along the pool surface, i.e., $\overline{BC}$ in Figure 3.1(a), are obtained by interpolation from the centerplane pool surface profile prior to transition. Then a circular cylindrical bubble is created with its center at the same location as the center of the three-dimensional bubble before the transition. The values of (x,y) for vertices along the bubble interface are then easily computed as the intersection points in Figure 3.5. With (x,y) now chosen on the bubble interface as well as along the pool surface, the iterative procedure in connection with Equations (3-25) can be employed to generate the entire mesh.

The second step is to create a (u,v) field for the SURGE code to carry on the flow simulation. The values of (u,v) along pool surface are obtained by interpolation from the (u,v) distribution along the centerplane pool surface in SWELL3 calculation prior to the transition. Along the circular bubble interface, the velocity is assumed to be uniformly expanding outward, as shown in Figure 3.5, and (u,v) are just the components of these vectors. The magnitude of these diverging vectors is the same for each vertex on the interface, and it is so chosen that the resulting volumetric expansion rate, $d\tilde{V}_B/dt$, of the cylindrical bubble is the same as $d\tilde{V}_B/dt$ before the transition. The values (u,v) associated with the rest of the mesh points are found by noting that, for two-dimensional incompressible irrotational flows, u and v satisfy the Laplace equation, viz.

$$\frac{\partial^2 Q}{\partial x^2} + \frac{\partial^2 Q}{\partial y^2} = 0 \tag{3-30}$$

where Q = u or v. Using the coordinate transformations

$$\frac{\partial Q}{\partial x} = \left(\frac{\partial y}{\partial b}\frac{\partial Q}{\partial a} - \frac{\partial y}{\partial a}\frac{\partial Q}{\partial b}\right) / J \tag{3-31}$$

$$\frac{\partial Q}{\partial y} = -\left(\frac{\partial x}{\partial b}\frac{\partial Q}{\partial a} - \frac{\partial x}{\partial a}\frac{\partial Q}{\partial b}\right) / J \tag{3-32}$$

(J is the Jacobian defined in Equation (3-28)), Equation (3-30) can be written in the Lagrangian (a,b) space as

$$\alpha^*\left(\frac{\partial^2 x}{\partial a^2}\right) + \beta^*\left(\frac{\partial^2 Q}{\partial a \partial b}\right) + \gamma^*\left(\frac{\partial^2 Q}{\partial b^2}\right) + \left[-\left(\frac{\partial y}{\partial b}\right)A + \left(\frac{\partial x}{\partial b}\right)B\right]\left(\frac{\partial Q}{\partial a}\right) / J$$

$$+ \left[\left(\frac{\partial y}{\partial a}\right)A - \left(\frac{\partial x}{\partial a}\right)B\right]\left(\frac{\partial Q}{\partial b}\right) / J = 0 \tag{3-33}$$

where

$$A \equiv \alpha^*\left(\frac{\partial^2 x}{\partial a^2}\right) + \beta^*\left(\frac{\partial^2 x}{\partial a \partial b}\right) + \gamma^*\left(\frac{\partial^2 x}{\partial b^2}\right) = 0$$

$$B \equiv \beta^*\left(\frac{\partial^2 y}{\partial a^2}\right) + \beta^*\left(\frac{\partial^2 y}{\partial a \partial b}\right) + \gamma^*\left(\frac{\partial^2 y}{\partial b^2}\right) = 0$$

by virtue of Equations (3-23). Equation (3-33) then reduces to

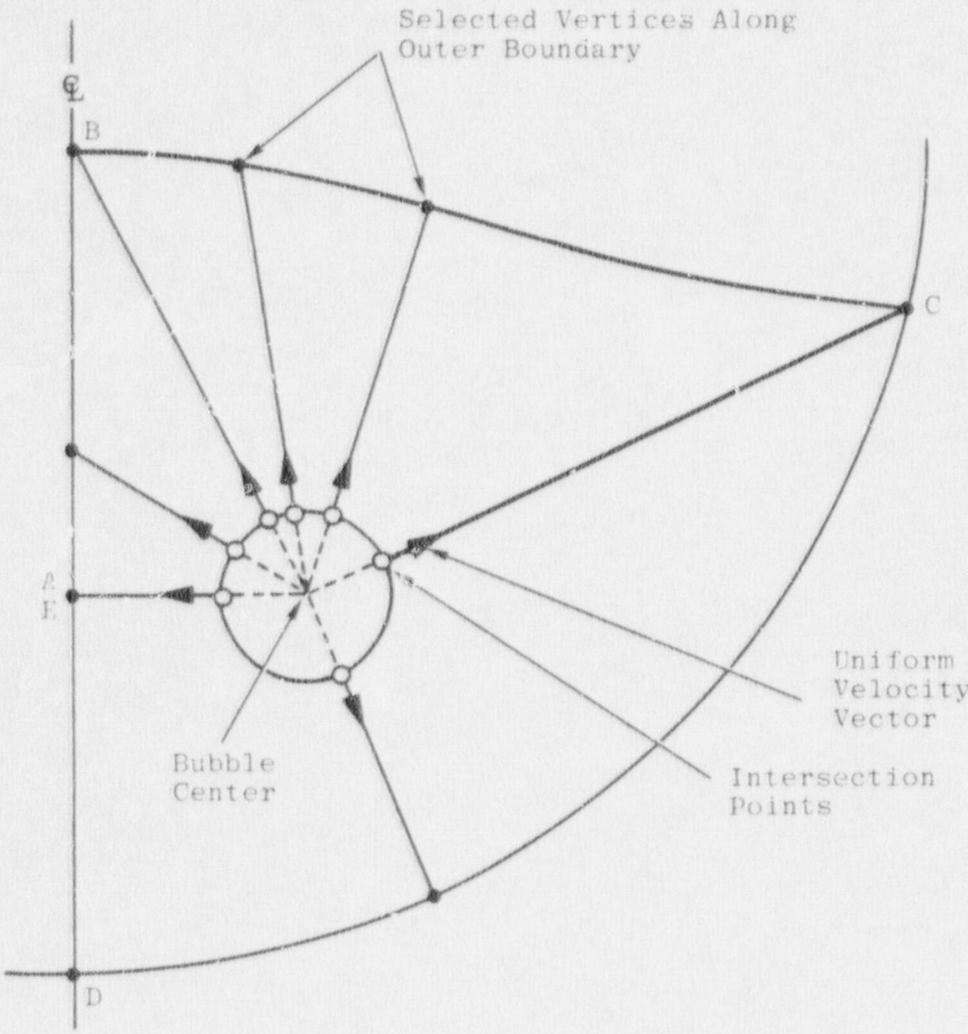

Figure 3.5. Generation of Initial Conditions for a SURGE Run

$$\alpha^*\left(\frac{\partial^2 \rho}{\partial a^2}\right) + \beta^*\left(\frac{\partial^2 \rho}{\partial a \partial b}\right) + \gamma^*\left(\frac{\partial^2 \rho}{\partial b^2}\right) = 0 \tag{3-34}$$

which is identical in form to Equations (3-23), and therefore can be solved by the same iterative procedure described in connection with Equations (3-25). In addition to pool and bubble surfaces, other boundary conditions need to be imposed. Referring to Figure 3.5, along the line of symmetry $\overline{AB}$ and $\overline{DE}$, and along the torus wall $\overline{CD}$, the following conditions are imposed:

$$u\left(\frac{\partial y}{\partial a}\right) - v\left(\frac{\partial x}{\partial a}\right) = 0 \tag{3-35}$$

$$\frac{\partial u}{\partial y} - \frac{\partial v}{\partial x} = 0 \tag{3-36}$$

Equation (3-35) states that the velocity component normal to the boundary vanishes and Equation (3-36) requires zero vorticity at the wall. By using the relations in Equations (3-31) and (3-32), Equation (3-36) becomes

$$-\left(\frac{\partial x}{\partial b}\right)\left(\frac{\partial u}{\partial a}\right) + \left(\frac{\partial x}{\partial a}\right)\left(\frac{\partial u}{\partial b}\right) - \left(\frac{\partial y}{\partial b}\right)\left(\frac{\partial v}{\partial a}\right) + \left(\frac{\partial y}{\partial a}\right)\left(\frac{\partial v}{\partial b}\right) = 0 \tag{3-37}$$

Using the index system in Figure 3.3, the finite-difference forms of Equations (3-35) and (3-37), respectively, are

$$u_{ij}\, y_a - v_{ij}\, x_a = 0 \tag{3-38}$$

$$-\frac{x_b}{2}\,(u_{i+1j} - u_{i-1j}) + x_a\,(u_{ij} - u_{ij-1}) - \frac{y_b}{2}\,(v_{i+1j} - v_{i-1j})$$

$$+\, y_a\,(v_{ij} - v_{ij-1}) = 0 \tag{3-39}$$

where

$$x_a = (x_{i+1j} - x_{i-1j})/2$$

$$y_a = (y_{i+1j} - y_{i-1j})/2$$

$$x_b = x_{ij} - x_{ij-1}$$

$$y_b = y_{ij} - y_{ij-1}$$

Solving Equations (3-38) and (3-39) simultaneously, we obtain

$$\left.\begin{aligned} u_{ij} &= G \cdot x_a \\ v_{ij} &= G \cdot y_a \end{aligned}\right\} \tag{3-40}$$

where

$$G = \left[\frac{x_b}{2}\left(u_{i+1j} - u_{i-1j}\right) + x_a\, u_{ij-1} + \frac{y_b}{2}\left(v_{i+1j} - v_{i-1j}\right) + y_a\, v_{ij-1}\right] / \left(x_a^2 + y_a^2\right)$$

Equations (3-40) are the iteration formulas for satisfying the boundary conditions along the solid boundaries. They are imposed repeatedly during the iterative soluation of Equation (3-34) for (u,v).

3.4 SOLUTION OF THE PRESSURE FIELD

To obtain forces on the torus wall, one needs to know the pressure distribution along the boundary. This objective can be met by obtaining the pressure associated with the vertices, rather than that defined at cell centers. In SURGE, a Poisson equation, i.e.,

$$\frac{\partial^2 p^*}{\partial x^2} + \frac{\partial^2 p^*}{\partial y^2} = -\rho\left[\frac{\partial^2 (u^2)}{\partial x^2} + 2\,\frac{\partial^2 (uv)}{\partial x \partial y} + \frac{\partial^2 (v^2)}{\partial y^2}\right], \tag{3-41}$$

is used to compute vertex pressures p^* from the (u,v) field. In Equation (3-41) ρ is the density of water. Using Equations (3-31) and (3-32) for evaluating derivatives and the left side of Equation (3-33) for the Laplacian operator in the (a,b) space, Equation (3-41) can be discretized using finite difference and solved by successive over-relaxation. The appropriate boundary conditions are the following: At the pool surface p^* is set equal to the current airspace pressure and it is set equal to the current bubble pressure at the bubble interface. At a solid boundary, consider the momentum equations in rectangular cartesian coordinates:

$$\frac{\partial u}{\partial t} + \frac{\partial (u^2)}{\partial x} + \frac{\partial (uv)}{\partial y} = -\frac{1}{\rho}\frac{\partial p^*}{\partial x} + g_x \tag{3-42}$$

$$\frac{\partial v}{\partial t} + \frac{\partial (uv)}{\partial x} + \frac{\partial (v^2)}{\partial y} = -\frac{1}{\rho}\frac{\partial p^*}{\partial y} + g_y \tag{3-43}$$

where (g_x, g_y) are the components of the gravitational acceleration. At a solid boundary (Figure 3.3), the acceleration normal to the wall is zero, thus

$$\frac{\partial u}{\partial t}\sin\theta - \frac{\partial v}{\partial t}\cos\theta = 0 \tag{3-44}$$

Substituting Equations (3-42) and (3-43) into Equation (3-44) and using the transformations in Equation (3-31) and (3-32), we obtain

$$\gamma^*\left(\frac{\partial p^*}{\partial b}\right) + \frac{\beta^*}{2}\left(\frac{\partial p^*}{\partial a}\right) = \rho\ S \tag{3-45}$$

with

$$S = \left(\frac{\partial y}{\partial a}\right)\left[\frac{\partial y}{\partial b}\frac{\partial (u^2)}{\partial a} - \frac{\partial y}{\partial a}\frac{\partial (u^2)}{\partial b} - \frac{\partial x}{\partial b}\frac{\partial (uv)}{\partial a} + \frac{\partial x}{\partial a}\frac{\partial (uv)}{\partial b}\right]$$

$$- \left(\frac{\partial x}{\partial a}\right)\left[\frac{\partial y}{\partial b}\frac{\partial (uv)}{\partial a} - \frac{\partial y}{\partial a}\frac{\partial (uv)}{\partial b} - \frac{\partial x}{\partial b}\frac{\partial (v^2)}{\partial a} + \frac{\partial x}{\partial a}\frac{\partial (v^2)}{\partial b}\right] .$$

Here β^* and γ^* have the same definitions as in Equations (3-23). In finite difference form, Equation (3-45) becomes

$$p^*_{ij} = p^*_{ij-1} + \frac{1}{\gamma^*}\left[\rho\ S_{ij} - \frac{\beta^*}{4}\left(p^*_{i+1j} - p^*_{i-1j}\right)\right] \tag{3-46}$$

This equation is the iteration formula for boundary condition of p^* at a rigid boundary.

Section 4

MODEL FOR FLOW IN THE VENT SYSTEM AND BUBBLES

A model for compressible gas flow in the vent system and bubble is described in this section. Our approach is to use a simple model which possesses the essential features of the phenomena that concern us. Further refinement will be made only after we fully understand the role of various factors in the model. Thus, our present vent flow model assumes an adiabatic gas flow in a pipe of constant cross-sectional area. The energy loss is represented by a nominal fL/D factor, which is uniformly distributed along the length of the pipe. Furthermore, the gas flow in the vent pipe is assumed to be in quasi-steady state.

4.1 DERIVATION OF GOVERNING EQUATIONS

The subject under consideration consists of two parts: the gas flow in the vent pipe and the gas in the bubbles. These models are essentially the same as those used by Moody [7]. First, consider the equation governing the pressure in a compressible bubble. Let M_B, $\tilde{V}_B$, T_B, E_B, and p_B be the mass, volume, temperature, internal energy, and pressure, respectively, associated with the gas in the bubble. The physical situation is depicted in Figure 4.1.

Assuming a perfect gas, one can write the following relations:

$$\text{Perfect Gas Law} \qquad p_B \tilde{V}_B = M_B R T_B , \tag{4-1}$$

$$\text{Internal Engery} \qquad E_B = M_B C_v T_B , \tag{4-2}$$

where R is the gas constant and C_v is the specific heat at constant volume.

Eliminating $M_B T_B$ between Equations (4-1) and (4-2), we obtain

$$p_B \tilde{V}_B = R E_B/C_v$$

or, upon differentiating with respect to time,

$$\frac{d}{dt} (p_B \tilde{V}_B) = \frac{R}{C_v} \frac{dE_B}{dt} = (\gamma - 1) \frac{dE_B}{dt} , \tag{4-3}$$

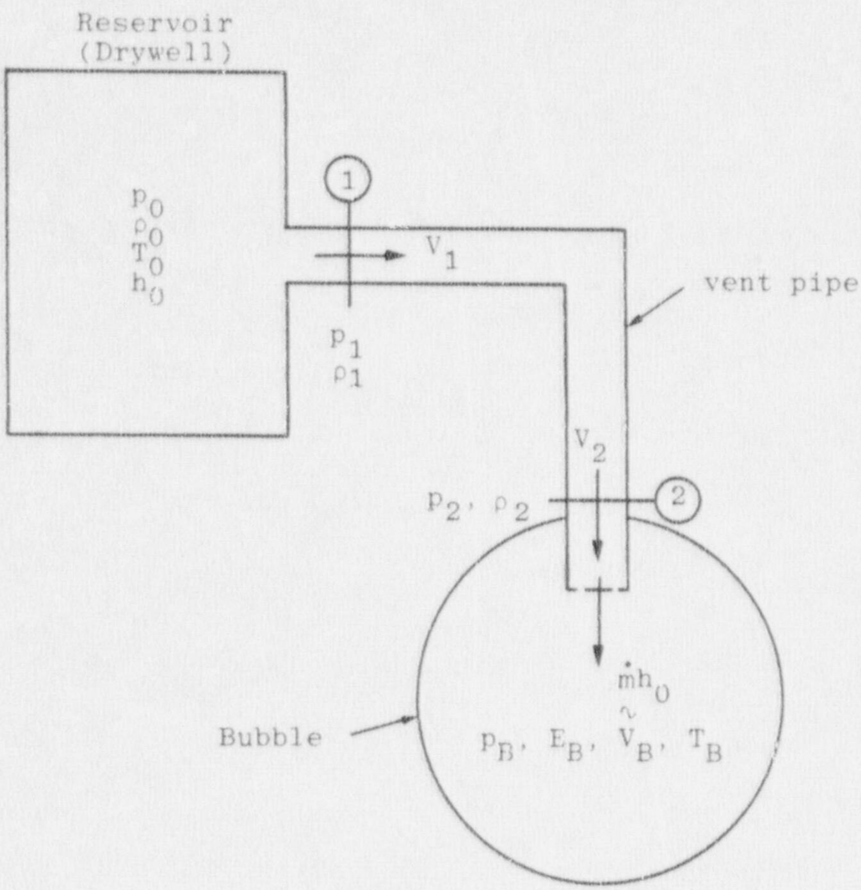

Figure 4.1. Schematic of the Compressible Gas Flow Model

where γ is the specific heat ratio. By considering the energy balance in the bubble, one can write

$$\frac{dE_B}{dt} = -p_B \frac{d\tilde{V}_B}{dt} + \dot{m} h_0 \quad . \tag{4-4}$$

The first term on the right side of Equation (4-4) is the rate of work done by the gas in the bubble, and the second term is the enthalpy flux into the bubble through the pipe. Here, h_0 is the stagnation enthalpy and $\dot{m}$ is the mass flow rate in the pipe. In this formulation, we have neglected the energy dissipation and kinetic energy inside the bubble and the heat transfer occurring at the bubble surface. Effects of these variables are expected to be small.

Now, referring to Figure 4.1, let p_0, ρ_0, and T_0 be the pressure, density, and temperature in the drywell, respectively. For a perfect gas, $h_0 = [\gamma/(\gamma-1)](p_0/\rho_0)$. Using this relation and substituting Equation (4-4) into Equation (4-3), we have

$$\frac{dp_B}{dt} = \frac{\gamma}{\tilde{V}_B}\left(\frac{p_0}{\rho_0}\dot{m} - p_B \frac{d\tilde{V}_B}{dt}\right) \quad . \tag{4-5}$$

This is the governing equation for pressure in the bubble. The mass flow rate $\dot{m}$ will be expressed below in terms of other quantitites in the vent system.

Assuming isentropic process between reservoir and point 1, we can write

$$p_1 = p_0 \left[1 + \frac{\gamma - 1}{2} M_1^2\right]^{-[\gamma/(\gamma-1)]} \tag{4-6}$$

$$\rho_1 = \rho_0 \left[1 + \frac{\gamma - 1}{2} M_1^2\right]^{-[1/(\gamma-1)]} \tag{4-7}$$

For a perfect gas in any process, the fluid velocity V_1 can be written in terms of Mach number M_1 by

$$V_1 = M_1 \sqrt{\frac{\gamma p_1}{\rho_1}}$$

Because of the steady-state assumption, the mass flux in the vent pipe is given by

$$\dot{m} = \rho_1 V_1 A \quad , \tag{4-9}$$

where A is the constant cross-sectional area and V_1 is the average flow speed at point 1 near the pipe entrance (Figure 4.1). Eliminating p_1, ρ_1, and V_1 among Equations (4-6) through (4-9), the result is

$$\dot{m} = \frac{M_1 A \sqrt{\gamma p_0 \rho_0}}{\left[1 + \frac{\gamma - 1}{2} M_1^2\right]^{(\gamma+1)/[2(\gamma-1)]}} \qquad (4\text{-}10)$$

Using this expression for $\dot{m}$ in Equation (4-5), we finally have

$$\frac{dp_B}{dt} = \frac{\gamma}{\tilde{V}_B} \left\{ \frac{M_1 p_0 A \sqrt{\gamma p_0/\rho_0}}{\left[1 + \frac{\gamma - 1}{2} M_1^2\right]^{(\gamma+1)/[2(\gamma-1)]}} - p_B \frac{d\tilde{V}_B}{dt} \right\} . \qquad (4\text{-}11)$$

For adiabatic flow in a duct of constant area, we also have the relation [8]:

$$\frac{p_B}{p_1} = \frac{M_1}{M_2} \sqrt{\frac{1 + \frac{\gamma - 1}{2} M_1^2}{1 + \frac{\gamma - 1}{2} M_2^2}} \qquad (4\text{-}12)$$

In this equation, we have substituted p_B for p_2, since it has been confirmed experimentally that these two pressures are practically the same for the flow regime considered here. Combining Equations (4-6) and (4-12), we have

$$\frac{p_B}{p_0} = \frac{M_1}{M_2} \sqrt{\frac{\left[1 + \frac{\gamma - 1}{2} M_1^2\right]^{(1+\gamma)/(1-\gamma)}}{1 + \frac{\gamma - 1}{2} M_2^2}} \qquad (4\text{-}13)$$

Finally, if the energy loss is uniformly distributed along the pipe, we have [8]

$$\frac{fL}{D} = \frac{1}{\gamma}\left(\frac{1}{M_1^2} - \frac{1}{M_2^2}\right) + \left(\frac{\gamma + 1}{2\gamma}\right) \ln \left[\left(\frac{M_1}{M_2}\right)^2 \cdot \frac{(\gamma - 1)\ M_2^2 + 2}{(\gamma - 1)\ M_1^2 + 2}\right] \qquad (4\text{-}14)$$

where the nominal loss factor fL/D must be specified for each problem.

Equations (4-11), (4-13), and (4-14) constitute the set of equations that model the compressible gas flow in the vent pipe and bubbles. The unknowns to be solved are p_B, M_1, and M_2, the other quantities being given at any instant of time. In fact, γ, fL/D, p_0, ρ_0, and A are a part of the parameters that define the problem, while $\tilde{V}_B$ and $d\tilde{V}_B/dt$ are the results of solving the time-dependent flow in the pool.

4.2 NUMERICAL SOLUTION PROCEDURE

For p_B/p_0 in the range $0.7 \leq p_B/p_0 \leq 1.0$, a very simple, but accurate, expression may be derived from Equations (4-13) and (4-14):

$$M_1^2 = \frac{1 - (p_B/p_0)^2}{\gamma\left(1 + \frac{fL}{D}\right)} \tag{4-15}$$

This equation is obtained by making series expansions in M_1^2 and neglecting higher-order terms. Note that M_2 is no longer present in Equation (4-15). Similarly, for small M_1^2 we can make the approximation

$$\left[1 + \frac{\gamma - 1}{2} M_1^2\right]^{(\gamma+1)/[2(\gamma-1)]} \approx 1 + \left(\frac{\gamma + 1}{4}\right) M_1^2$$

and reduce Equation (4-11), with the aid of Equation (4-15), to the form

$$\frac{dP_B}{dt} = \frac{\gamma}{\tilde{V}_B} \left\{ \frac{p_0 \; M_1 \; A\sqrt{\gamma p_0/\rho_0}}{1 + \left(\frac{\gamma+1}{4}\right) M_1^2} - p_B \frac{d\tilde{V}_B}{dt} \right\}$$

$$= \frac{\gamma}{\tilde{V}_B} \left\{ \frac{p_0 \; A\sqrt{\gamma p_0/\rho_0} \; \sqrt{[1 - (p_B/p_0)^2]/[\gamma(1 + \frac{fL}{D})]}}{1 + \left(\frac{\gamma+1}{4}\right) [1 - (p_B/p_0)^2]/[\gamma(1 + \frac{fL}{D})]} - p_B \frac{d\tilde{V}_B}{dt} \right\} \tag{4-16}$$

Using the superscript n to denote the time level; e.g., $t^{n+1} - t^n = (\delta t)^n$ where $(\delta t)^n$ is the time increment, Equation (4-16) is discretized as

$$\frac{p_B^{n+1} - p_B^n}{(\delta t)^n}$$

$$= \frac{\gamma}{(\tilde{V}_B)^n} \left\{ \frac{p_0^{n+1} \; A\sqrt{\gamma \; p_0^{n+1}/\rho_0^{n+1}} \; \sqrt{[1 - (p_B^{n+1}/p_0^{n+1})^2]/[\gamma(1 + \frac{fL}{D})]}}{1 + \left(\frac{\gamma+1}{4}\right) [1 - (p_B^{n+1}/p_0^{n+1})^2]/[\gamma(1 + \frac{fL}{D})]} \right.$$

$$\left. - (p_B)^{n+1} \left(\frac{d\tilde{V}_B}{dt}\right)^n \right\} \tag{4-17}$$

Equation (4-17) is in "implicit" form because every term on the right-hand side is evaluated at the advanced time level n+1, with $\tilde{V}_B$ and $d\tilde{V}_B/dt$ as the only exceptions. Though one could also evaluate these quantities at the new time level, it was found by actual calculations that the results are practically the same if they were evaluated at the old time level. One advantage of this "explicit" treatment of $\tilde{V}_B$ and $d\tilde{V}_B/dt$ is that they can be easily computed from the geometry and motion of the bubble at the old time level, thus avoiding the need to iterate between p_B^{n+1} and the hydrodynamics in the pool.

In performing stepwise time-integration, Equation (4-17) reduces to the problem of finding a value for p_B^{n+1} such that $F(p_B^{n+1}) = 0$, since all other quantities are known. The Newton-Raphson method may be used for this purpose. The iterative formula is

$$(p_B^{n+1})^{(\nu+1)} = (p_B^{n+1})^{(\nu)} - F[(p_B^{n+1})^{(\nu)}]/F'[(p_B^{n+1})^{(\nu)}] \qquad (4\text{-}18)$$

where ν is the iteration number and F' is the first derivative of F. Because the bubble pressure does not change much during one time step, a good first approximation for initiating the iteration is to use p_B^n for p_B^{n+1}; i.e., $(p_B^{n+1})^{(1)} = p_B^n$. Equation (4-18) is then used repeatedly until the correction to p_B^{n+1} becomes less than a prescribed amount.

The procedure above is used after vent clearing. Before the vent clears, the pressure exerting on the water surface inside the downcomer is set equal to the drywell pressure, since in this period the velocity of gas in the vent system is quite small and the corresponding pressure drop is negligible.

Section 5

SAMPLE CALCULATION

A computation of the pool response during an experimentally controlled loss of coolant accident in a 1/4-scale test facility was made using the SWELL3 and SURGE computer programs. The data for this calculation is from the 1/4-scale test run, Part 1 Test 21, supplied by the General Electric Company (Case GE 1-21). The results of the computations are shown in Figures 5.1 through 5.4.

Figure 5.1 gives a three-dimensional perspective view of the water in the pool at various times during the bubble growth phase after the clearing of the downcomers, as calculated by SWELL3. At 0.182 second after the initiation of drywell pressurization when the bubbles are large enough so that the solution on the wall of the torus is essentially two-dimensional, that is, there is little variation in the transverse or y direction, then a transition is made from the three-dimensional SWELL3 model to the two-dimensional SURGE model. This is accomplished by assuming that the bubbles have a circular cross section with uniform radial velocity determined so that the mass flow rate matches that through the bubbles from SWELL3 at transition. The pool surface velocities and displacements are also transferred from SWELL3 to SURGE. Figure 5.2 shows the pool motion from the time of transition to the time of ring header impact as predicted by the SURGE model.

Combined results from SURGE and SWELL3 from time of initiation of drywell pressurization to the instant of ring header impact are shown in Figure 5.3. These results include the experimental drywell pressure history used as input, the resulting bubble pressure, wetwell airspace pressure, and torus pressures at the far bottom of the pool; i.e., 180°, and on the sides of the pool at 210° and 240°. Also shown are the dynamic load and impulse on the torus. Figure 5.4 gives the bubble and pool surface profiles as well as velocities at selected points on the pool surface as computed by SURGE.

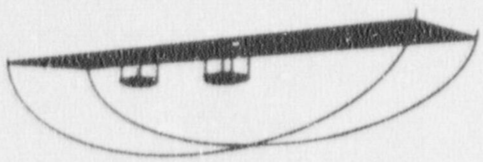

t = 0.154 Sec. (Vent Clearing)

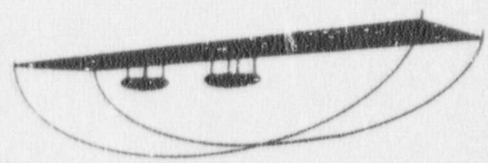

t = 0.160 Sec.

t = 0.168 Sec.

t = 0.182 Sec., Transition to SURGE

Figure 5.1. Bubble and Pool Surface Plots from SWELL3 for Case GE 1-21

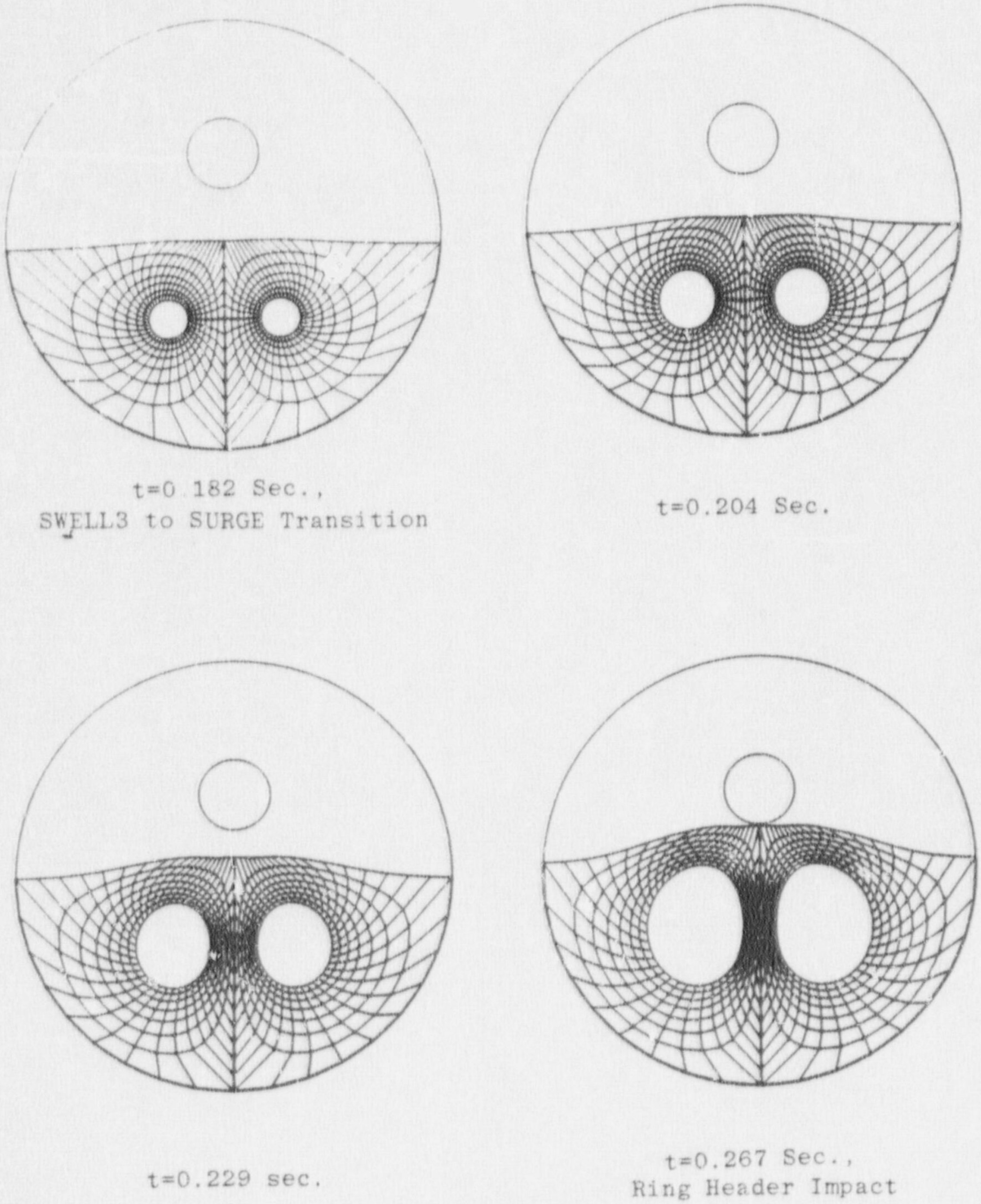

Figure 5.2. Bubble and Pool Surface Plots from SURGE for Case GE 1-21

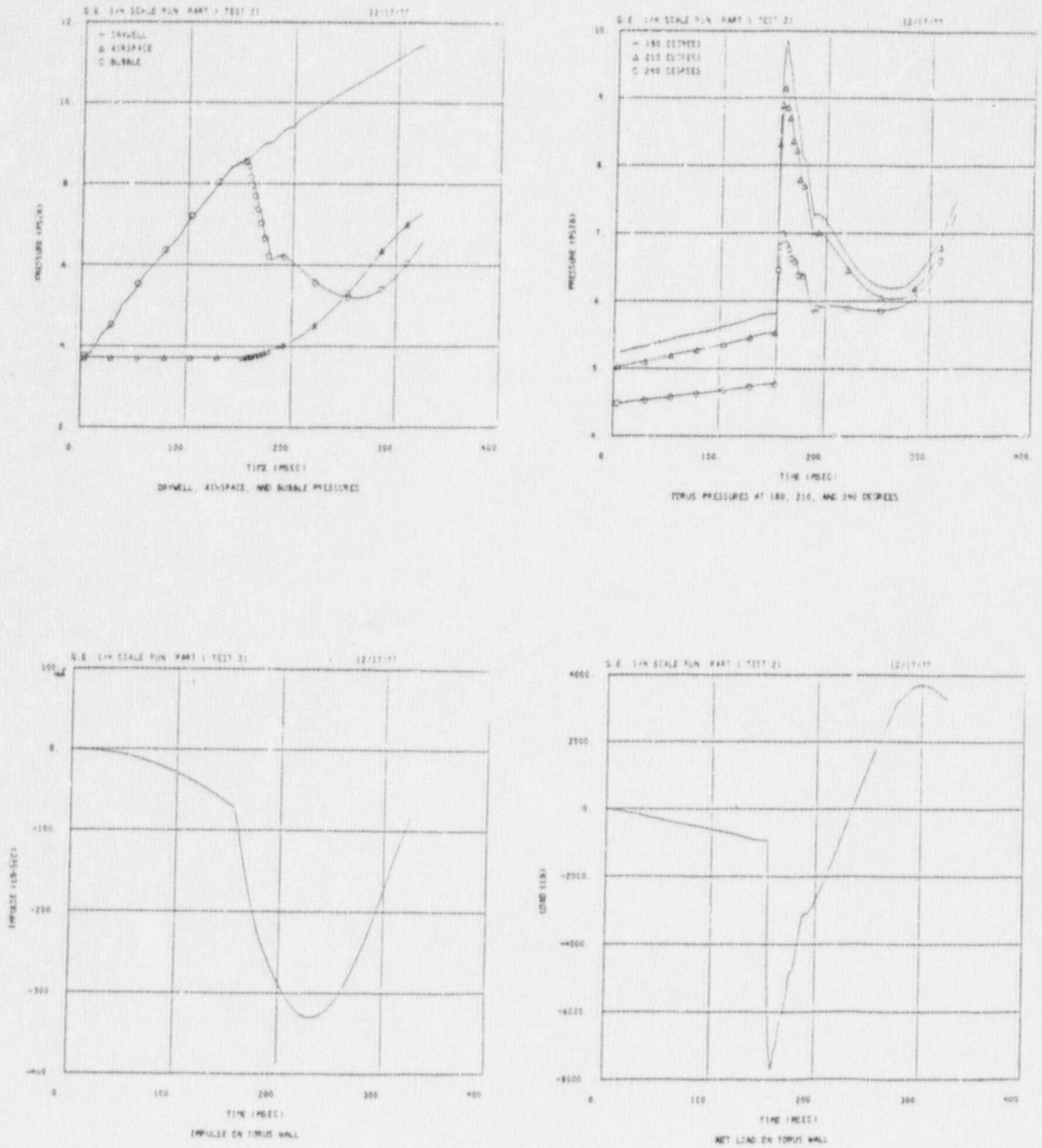

Figure 5.3. Pressures, Load, and Impulse for Case GE 1-21

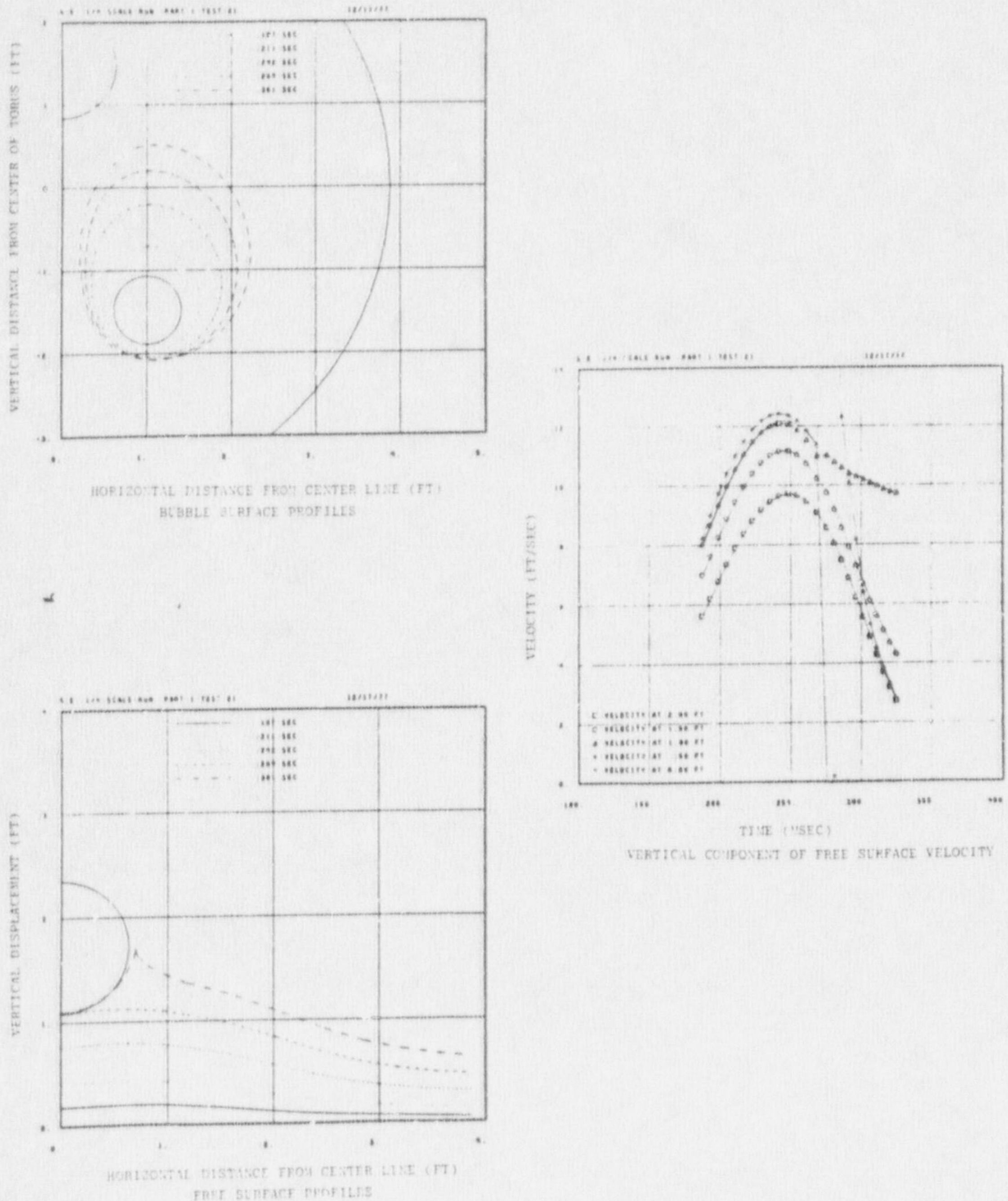

Figure 5.4. Pool Surface Displacements, Bubble Surface Profiles, and Pool Surface Velocities from SURGE for Case GE 1-21

Section 6

REFERENCES

1. Chan, R. K.-C., Kuo, H.-H., and Nakayama, P. I., Numerical Simulation of Hydrodynamic Response of MARK I Suppression Pools, EPRI NP-345, Key Phase Report, January 1977.

2. Chan, R, K.-C. and Street, R. L., A Computer Study of Finite-Amplitude Water Waves, J. Comp. Phys., 6, 68-94, 1970.

3. Vander Vorst, M. J. and Van Tuyl, A. J., Calculation of Incompressible Underwater Bubble Phenomena by the Marker and Cell Method, Proceedings of the First International Conference on Numerical Ship Hydrodynamics, David W. Taylor Naval Ship Research and Development Center, Bethesda, MD, 1975.

4. Knuth, D. E., The Art of Computer Programming, Volume 1, Fundamental Algorithms, Addison-Wesley Publishing Company, 1968.

5. Chan, R. K.-C., A Generalized Arbitrary Lagrangian-Eulerian Method for Incompressible Flows with Sharp Interfaces, J. Comp. Phys., 17, 311-331, 1975.

6. Thompson, J. F., Thames, F. C., and Mastin, C. W., Automatic Numerical Generation of Body-Fitted Curvilinear Coordinate System for Field Containing Any Number of Arbitrary Two-Dimensional Bodies, J. Comp. Phys., 15; 299-319, 1974.

7. Moody, F. J., private communication, General Electric Company.

8. Streeter, V. L., Fluid Mechanics, Section 6.6, McGraw-Hill, New York, 1962.

Appendix A-1

SUCCESSIVE OVER-RELAXATION

Successive over-relaxation (SOR) is an effective and easily programmed iterative method to solve the system of linear algebraic equations which arise from the discretization of Laplace's or more generally Poisson's equation. The method is most useful in transient problems where a good initial guess is available from the solution at the previous time step. Varga* gives a complete development of the method. Vander Vorst** gives a discussion of the implementation of SOR to hydrodynamic problems with emphasis on the development of a criteria for stopping the iteration after a predetermined accuracy has been obtained.

Finite difference approximations to Poisson's equation on a three-dimensional mesh give rise to a system of equations, each of which is of the form

$$\begin{aligned} & c_1 \phi_{i,j,k-1} + c_2 \phi_{i,j-1,k} + c_3 \phi_{i-1,j,k} + d \phi_{i,j,k} \\ & + c_4 \phi_{i+1,j,k} + c_5 \phi_{i,j+1,k} + c_6 \phi_{i,j,k+1} \\ & = S_{i,j,k} \end{aligned} \tag{A1-1}$$

where each of the coefficients depends on (i,j,k).

The SOR method for solving the system (A1-1) is given by the following algorithm:

---

*R. S. Varga, Matrix Iterative Analysis, Prentice-Hall, Inc., New Jersey, 1962.

**M. J. Vander Vorst, "A Survey of Error Estimates for Iterative Solutions of Systems of Linear Equations," Naval Ordnance Laboratory, NOLTR 72-18%, October 1972.

$m = 0$

<u>until</u> $e^m < e$

$\tilde{e} = 0$

<u>for</u> $k = 1$ to K_{max}

<u>for</u> $j = 1$ to J_{max}

<u>for</u> $i = 1$ to I_{max}

$$\tilde{\phi}_{i,j,k} = \frac{1}{d}\Big[S_{i,j,k} - c_1\,\phi^{m+1}_{i,j,k-1} - c_2\,\phi^{m+1}_{i,j-1k} - c_3\,\phi^{m+1}_{i-1,j,k} - c_4\,\phi^{m}_{i+1,j,k} - c_5\,\phi^{m}_{i,j+1,k} - c_6\,\phi^{m}_{i,j,k+1}\Big]$$

$$\phi^{m+1}_{i,j,k} = \phi^{m}_{i,j,k} + \omega(\tilde{\phi}_{i,j,k} - \phi^{m}_{i,j,k})$$

$$\tilde{e} = \tilde{e} + (\phi^{m+1}_{i,j,k} - \phi^{m}_{i,j,k})^2$$

<u>end</u> i,j,k

$m = m + 1$

$$e^m = \sqrt{\tilde{e}/\Sigma(\phi^{m}_{i,j,k})^2}$$

<u>end</u>

Sufficient conditions for convergence of the above algorithm are given in Varga. When these conditions are satisfied, there is an optimum SOR factor, ω,

$$1 < \omega < 2 \ ,$$

independent of the source term, $S_{i,j,k}$, which gives the fastest asymptotic convergence of ϕ^m to the solution ϕ of the linear system. These conditions will not be given here, however, we note that (2-24) satisfies them while (2-29) does not. We have found, however, that the system converges if we underrelax the torus wall boundary condition (2-29), i.e., use $0 < \omega < 1$, or in our case $\omega = 0.4$. The order in which the equations are solved within a single iteration is also important. The ordering used in the above algorithm, <u>the natural ordering</u>, satisfies the conditions for convergence. However for programming convenience, the order used in the SWELL3 code is to first solve the interior equations, including irregular stars, using the natural ordering, then solve the rigid wall and pool surface boundary equations. The iteration still converges although probably at a slower rate.

In order to attain maximum efficiency in the code, we wish to use a value for ω as close as possible to the optimum. To numerically determine a value for near the optimum, we first need to quantify the concept of convergence rate. Let the norm of ϕ be

$$|| \phi || = \sqrt{\Sigma(\phi_{i,j,k})^2} \quad ,$$

then the error, e^m, is

$$e^m = || \phi - \phi^m ||$$

and the difference, δ^m, between iterations is

$$\delta^m = || \phi^m - \phi^{m-1} || \quad .$$

Varga, shows that there is a constant, c, such that

$$|| \phi - \phi^m || \leq c \, || \phi^m - \phi^{m-1} || \quad .$$

If we denote by r^m the ratio,

$$r^m = \frac{\delta^m}{\delta^{m-1}} \quad ,$$

then we obtain

$$\frac{e^m}{e^{m-1}} \leq r^m \quad .$$

Moreover we know that r^m has an asymptotic limit, r. Hence, asymptotically the number of iterations, N_r, necessary to decrease the error by 1/10 is

$$N_r = -1/\log r \quad .$$

To find an acceptable over-relaxation factor, ω, for the problem geometry shown in Figure 2.5, a series of tests were performed to find the solution of

$\nabla^2\phi = 0$	interior
$\frac{\partial\phi}{\partial n} = \eta$	solid boundaries
$\phi = 0$	pool surface, $z = z_0$
$\phi = g(z_{k_d} - z_0)$	exit of downcomer

The exact solution to both the analytic and finite difference form of these equations is

$$\phi_{i,j,k} = g(z_k - z_0) \quad .$$

The initial guess for all cases is

$$\phi = 0 \quad .$$

The results of these tests are shown in Table 1. Note that the convergence rate is usually highest during the early iterations.

Based on the results shown in Table 1, we used an ω of 1.98 for all of the quarter scale runs. In addition, we found that after attaining the solution of $\nabla^2\phi = 0$ at $t = 0$, that only 50 to 100 iterations were needed to give an accuarcy of about two digits at succeeding times. The time step, Δt^n, in these cases was determined using a Courant number, $f_{\Delta t}$, of

$$f_{\Delta t} = 0.15 \quad .$$

Table 1. Determination of Optimum Over-Relation Factor

ω	m	$\frac{\|\|\phi^m - \phi^{m-1}\|\|}{\|\|\phi^m\|\|}$	r^{m*}	$e^m = \|\phi^m_{2,2,2} - \phi_{2,2,2}\|$ $\phi_{2,2,2} = 116$	$\frac{e^{m*}}{e^{m-1}}$	N_r
1.75	100	.37		98		550 iterations
	200	.27	.73	75	.77	
	300	.18	.67	42	.56	
	400	.12	.67	28	.67	
	500	.079	.66	18	.64	
	600	.052	.66	11	.61	
	700	.034	.65	7	.64	
	800	.022	.65	3	.43	
	900	.015	.68	2	.66	
	1000	.010	.67			
1.90	100	.56		68		290 iterations
	200	.25	.45	31	.46	
	300	.11	.44	14	.45	
	400	.05	.45	4	.29	
	500	.023	.46	-		
1.95	100	.60		52		210 iterations
	200	.19	.32	17	.33	
	300	.066	.35	3	.18	
	400	.022	.33	-		
	500	.008	.36	-		
1.97	100	1.16		45		180 iterations
	200	.17	.15	10	.22	
	300	.05	.29	3	.30	
	400	.014	.28	-		
1.98	100	3.03		38		140 iterations
	200	.29	.10	11	.29	
	300	.05	.17	3	.27	
	400	.011	.22	-		
1.99	100	8.14		34		170 iterations
	200	1.90	.23	4	.12	
	300	.54	.28	-		
	400	.14	.26	-		

*per 100 iterations

Appendix A-2

FORMATION OF IRREGULAR STARS

The following procedure is used to find the irregular stars from the surface geometry:

```
Procedure stars
for each mesh point (i,j,k)
   if point inside region
   then if each of six neighbors, N_ℓ, are in region
      then point (i,j,k) is a "regular interior" point
      else point (i,j,k) is an "irregular interior"
         find length δ_ℓ of each leg
         find six coefficients for Laplacian (2-24)
      end
   else point is "out"
   end
end
end procedure
```

From the description of the above procedure, we see that we must determine whether each point (i,j,k) is inside or outside the region of the computations. Various solutions to this geometric problem are surveyed by Burton*. The procedure we use to determine whether the point, p, is inside a region, Ω, with rectifiable boundary, Γ, is to draw a ray, R, emanating from point p and count the number of intersections, N_R, of R passing through Γ. If N_R is odd, then p is inside Ω otherwise it is outside, as shown in the following illustration.

---

*W. Burton, "Representation of Many-Sided Polygonal Lines for Rapid Processing," Communications of ACM, Volume 20, Number 3, March 1977.

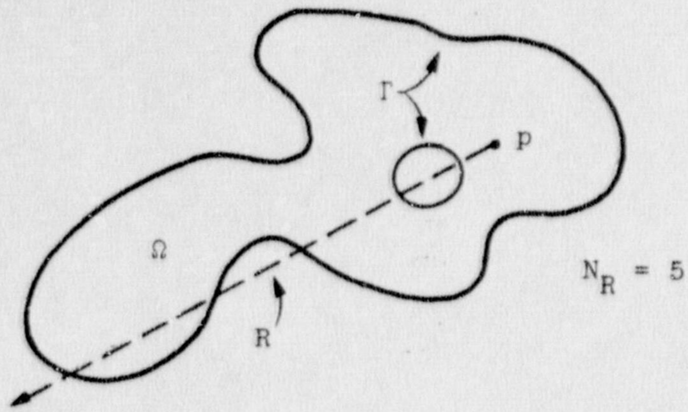

For a surface composed of triangular elements in three spatial dimensions we must determine whether R passes through each of the triangles. Moreover, this must be done for each mesh point or at least for those mesh points near the surface assuming that the others can be easily eliminated by a simple flagging scheme. In addition, if R intersects the triangle, Tq, on an edge, this intersection may be counted twice, once for Tq and once for an adjacent triangle. The probability that a ray will intersect precisely on the edge of a triangle is very remote given the properties of real arithmetic on a digital computer. Even so we account for this problem by considering not one ray, but three orthogonal rays, each normal to a coordinate plane. A by-product of using three such rays is the irregular star lengths needed to form the Laplacian operator, Equation (2-24).

If we were to examine each triangular surface segment for each mesh point near the surface, the number of computational operations needed to form the irregular stars far exceeds the number needed to solve the resulting system of linear equations. However, if the triangles are pre-processed such that for each cell (i,j,k) a list, $L_{i,j,k}$, of each of the triangles, Tq, intersecting the cell is made, then to determine the status of point (i,j,k) only the triangles associated with those cells containing the three rays need be examined. The resulting procedure to determine whether a mesh point is within the computational region and, if it is, to also find the irregular star is summarized below.

```
logical procedure isitin (i,j,k)
x′ = y′ = z′ = - ∞
for each Tq ∈ L_{i-1,j,k} ∪ L_{i,j,k} find closest intersection
     x′, x′ ≤ x_i, with the line (y = y_i, z = z_k) end
δx_{i-1} = min (x_i′ - x, Δx_{i-½})
for each Tq ∈ L_{i,j-1,k} ∪ L_{i,j,k} find closest intersection,
     y′, y′ ≤ y_i, with line (x = x_i, z = z_k) end
δy_{j-1} = min (y_j - y′, Δy_{j-½})
for each Tq ∈ L_{i,j,k-1} ∪ L_{i,j,k} find closest intersection,
     z′, z′ ≤ z_k, with line (x = x_i, y = y_j) end
δz_{k-1} = min (z_k - z′, Δz_{k-½})
isx = isy = isz = false
x̃ = ỹ = z̃ = ∞
for i′ = i to I_max
     for Tq ∈ L_{i′,j,k}
          if line (y = y_j, z = z_k) intersects Tq at x°
          then x̃ = min (x̃, x°)
               isx = ~isx
          end
     end
end
δx_{i+1} = min (x̃ - x_i, Δx_{i+½})
(similarly for j′ = j to J_max find δy_{j+1} and
     for k′ = k to K_max find δz_{k+1})
isitin = isx ∨ isy ∨ isz
end procedure
```

Appendix A-3

SOME GEOMETRIC IDENTITIES INVOLVING TRIANGLES

The plane determined by three points, $[p_1, p_2, p_3]$ in three-dimensional space (x_1, x_2, x_3) can be described as the locus of all points which satisfy

$$Ax_1 + Bx_2 + Cx_3 + D = 0 \quad , \tag{A3-1}$$

where $p_i = (x_{1i}, x_{2i}, x_{3i})$. However for our application it is more convenient to represent this plane using the parametric form

$$x_i = a_{i1}\,\alpha + a_{i2}\,\beta + a_{i3};\ i = 1, 2, 3 \tag{A3-2}$$

for all real pairs (α, β). This can be envisioned as a mapping from the triangle, $[p_1, p_2, p_3]$ formed by three points in three-dimensional space onto the unit triangle $[(0,0), (1,0), (0,1)]$ in the two-dimensional space (α, β) where

$$\begin{aligned} a_{i1} &= x_{i2} - x_{i1} \\ a_{i2} &= x_{i3} - x_{i1} \\ a_{i3} &= x_{i1} \end{aligned} \tag{A3-3}$$

Similarly the parametric equations for the line connecting two points, p_1 and p_2, in three-dimensional space can be written in one parameter

$$x_i = (1-\lambda)\,x_{i1} + \lambda\,x_{i2}$$

for all real numbers λ.

In the (α, β) space, the intersection of the line

$$\begin{aligned} x_i &= c_i \\ x_j &= c_j \\ i &\neq j \end{aligned} \tag{A3-4}$$

with the plane, (A3-2), is

$$\alpha' = \frac{(x_i - a_{i3})\, a_{j2} - (x_j - a_{j3})\, a_{i2}}{D}$$

$$\beta' = \frac{(x_i - a_{i3})\, a_{j1} - (x_j - a_{j3})\, a_{i1}}{D} \qquad \text{(A3-5)}$$

where

$$D = a_{i1}\, a_{j2} - a_{i2}\, a_{j1}$$

when

$$D \neq 0 \quad .$$

If D vanishes the line and the plane are parallel. In (x_1, x_2, x_3) space the solution is

$$x_i = c_i$$

$$x_j = c_j$$

$$x_k = a_{ki}\, \alpha' + a_{k2}\, \beta' + a_{k3}$$

$$i \neq j \neq k \quad . \qquad \text{(A3-6)}$$

The area of the triangle, T', formed by the three points, $[(\alpha_1, \beta_1), (\alpha_2, \beta_2), (\alpha_3, \beta_3)]$, in the two-dimensional space is

$$A(T') = \frac{1}{2}[\alpha_1 (\beta_2 - \beta_3) + \alpha_2 (\beta_3 - \beta_1) + \alpha_3 (\beta_1 - \beta_2)] \qquad \text{(A3-7)}$$

where $A(T')$ is positive when the points forming the triangle are enumerated in the counterclockwise direction and negative when numbered clockwise. The point of intersection (A3-6), of the line (A3-4), with the plane (A3-2), is within the triangles, T, formed by three points, $[P_1, P_2, P_3]$, if the point (α', β') from (A3-5) in the transformed space is within the unit triangle as shown below.

The point p_4 is within the triangle $T' = [p_1', p_2', p_3']$ if the areas, $A(T_1')$, $A(T_2')$, $A(T_3')$ of the three triangles

$$T_1' = [p_1', p_2', p_4']$$

$$T_2' = [p_2', p_3', p_4']$$

$$T_3' = [p_3', p_1', p_4']$$

are all non-negative, otherwise the point is outside the triangle.

Let the vector R be

$$R = \begin{bmatrix} x_1 (\alpha, \beta) \\ x_2 (\alpha, \beta) \\ x_3 (\alpha, \beta) \end{bmatrix}$$

where the x_i are from (A3-2). The area of the triangle, $T = [p_1, p_2, p_3]$, in physical space is given by the magnitude of the cross product

$$A(T) = \left| \frac{\partial R}{\partial \alpha} \times \frac{\partial R}{\partial \beta} \right|$$

or

$$A(T) = [(a_{21} a_{32} - a_{22} a_{31})^2 + (a_{12} a_{31} - a_{11} a_{32})^2$$

$$+ (a_{11} a_{22} - a_{12} a_{21})^2]^{\frac{1}{2}} .$$